J. Fluid Mech. (1999), vol. 383, pp. 143–173. Printed in the United Kingdom

Experiments on a barotropic rotating shear layer. Part 1. Instability and steady vortices

By WOLF-GERRIT FRÜH[1] AND PETER L. READ[2]

[1]Department of Mechanical and Chemical Engineering, Heriot-Watt University, Riccarton, Edinburgh, EH14 4AS, UK
[2]Department of Atmospheric, Oceanic and Planetary Physics, Clarendon Laboratory, University of Oxford, OX1 3PU, UK

(Received 24 September 1997 and in revised form 19 October 1998)

The barotropic shear layer in a rotating fluid is studied in a laboratory experiment. Through the rotation of circular sections in the base and lid of a circular tank relative to a background rotation of the entire system, a vertical layer of strong horizontal shear develops, the Stewartson layer. Above a critical shear, the shear layer breaks up through barotropic instability, which is an inertial instability. The flow then develops a string of vortices along the shear zone. It will be shown that the transition from an axisymmetric flow to regular vortices occurs through a Hopf bifurcation. Subsequent transitions to more complex flows, such as modulated vortices, chaos and highly irregular flow, will be presented briefly, while the main points of this paper are the primary instability, steady vortices and their nonlinear dynamics. Among the issues discussed is the sensitivity of the flow to the direction of the differential shear. The experimental data will be used to test the ability of boundary layer theory and quasi-geostrophic theory to predict the onset of instability and the range of unstable wavenumbers.

1. Introduction

1.1. *Outline*

Shear-driven instabilities in rotating fluids are fundamental problems in fluid dynamics. The instability studied here, sometimes called barotropic instability, is the instability of a rapidly rotating fluid subjected to a horizontal shear. When the shear across a thin region becomes sufficiently large, the shearing flow becomes unstable and the fluid tends to ‘roll up’ into vortices.

In this study, the nonlinear dynamics of the travelling vortices arising from the first instability and subsequent bifurcations are investigated. This paper mainly presents the global structure of the regime diagram, the instability of the basic axisymmetric flow, equilibration to steady vortices, and subsequent mode transitions. Secondary instabilities, such as the emergence of secondary oscillations and irregular flow are discussed in a future companion paper (Part 2). The observed dynamics and bifurcations are compared with those observed in related fluid experiments, such as a circular shear layer, baroclinic waves in a rotating annulus, and the Taylor–Couette system.

The remainder of § 1 gives some background to barotropic instability and previous studies of it. We will also mention some symmetry considerations in the context of expected bifurcations. After a description of the laboratory apparatus and experimental and analysis procedures in § 2, the results are presented. First the global structure of the regime diagram is discussed in § 3, followed by a discussion of the axisymmetric flow and its instability in § 4 and steady vortices in § 5. The final section, § 6, discusses the findings and puts them in context.

1.2. *Background*

Rotating shear layers occur in a variety of situations, from industrial to geophysical applications. An example of an industrial application is the design of computer hard disk drives (Humphrey & Gor 1993) where shear layers occur between the rapidly rotating magnetic disc and the stationary housing. Such shear layers are also an essential ingredient of the flow in the Earth's outer core which gives rise to the Earth's magnetic field (Hollerbach 1996). It has also been proposed that the prominent vortical features on the giant planets – of which the Great Red Spot on Jupiter is only the best known – are a result of barotropic instability, e.g. Meyers, Sommeria & Swinney (1989); Antipov *et al.* (1986); for alternative theories see Read (1992).

In the oceans and atmosphere, barotropic instability plays an essential role in the evolution of large-scale weather systems, such as at the end of the life cycle of baroclinic waves and fully developed fronts (Schär & Davies 1990; Simmons & Hoskins 1978), or in the breakup of tropical cyclones (Weber & Smith 1993). Recent laboratory experiments by Read *et al.* (1992) on baroclinic waves in a rotating fluid annulus which is subjected to a horizontal temperature gradient have suggested that some forms of 'structural vacillation' may be caused by a barotropic instability of the large-amplitude baroclinic wave. Structural vacillation is an oscillation of the wave shape, which at first sight seems regular, yet cannot be described by low-dimensional dynamics. Several studies (Früh & Read 1997; Guckenheimer & Buzyna 1983; Read *et al.* 1992) have found that estimates of the attractor dimensions for structural vacillation data did not converge to consistent results. Under certain conditions, when a structural vacillation solution coexists with another wave solution for the same forcing parameters, the small variation due to the structural vacillation may lead to a metastable system with irregular switching between the two solutions (Früh & Read 1997).

This study of the nonlinear dynamics of barotropic vortices aims at a better understanding of barotropically unstable systems and their relevance to observed flows in the laboratory and atmosphere. Since Rossby waves due to baroclinic instability have been shown to exhibit a rich variety of possible routes to low-dimensional chaos and to high-dimensional and possibly stochastic behaviour, the question arises of whether Rossby waves growing from an inertial instability of a rotating shear layer will show similar bifurcation scenarios. For instance, homoclinic orbits appeared to play a large role in the emergence of low-frequency modulations of baroclinic waves in the experiments by Früh & Read (1997). Frequency locking was also relatively common in the baroclinic annulus and had a very strong effect on the bifurcation sequences observed. For instance, evidence for period-doubling bifurcations was restricted to flows which were frequency locked in the sense that the wave drift and the wave amplitude had the same frequency, or frequencies with a simple integer ratio. A related issue is that of the effect of symmetries on bifurcation sequences. The baroclinic annulus and the system studied here have identical horizontal symmetries, the rotational invariance of the $SO(2)$ group, but different vertical symmetries. This raises the question of whether the horizontal or the vertical symmetry group is more important in the bifurcation structure.

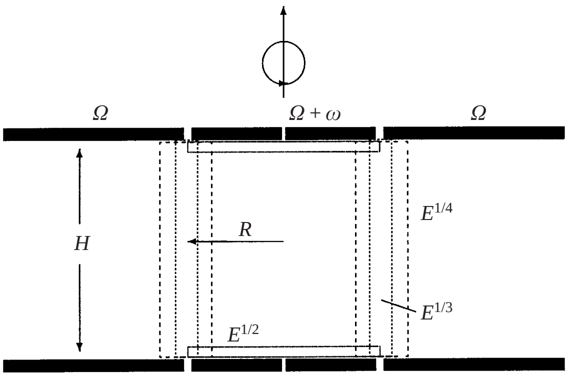

FIGURE 1. Stewartson layers after Stewartson (1957). The solid lines in the fluid domain indicate the Ekman layers while the inner, $E^{1/3}$, Stewartson layer is indicated by dotted lines and the outer, $E^{1/4}$, Stewartson layer by dashed lines.

1.3. *Previous laboratory studies*

The shear layer in a viscous rotating fluid was initially treated theoretically by Stewartson (1957); a uniform fluid with a background rotation Ω is bounded in the vertical by horizontal rigid boundaries separated by a distance H as shown in figure 1. A shear layer is forced by rotating sections of the lid and base at a rotation ω relative to the background rotation. Ekman layers form at the upper and lower boundaries carrying a mass transport proportional to $E^{1/2}$, which has to be balanced by a vertical transport in a shear region at the edge of the rotating sections. The resulting flow structures are two nested shear layers of thickness $E^{1/4}$ and $E^{1/3}$, the Stewartson layers.

A few laboratory experiments have addressed barotropic instability and resulting flow structures. Hide & Titman (1967) immersed a differentially rotating disk in a rotating fluid, which set up a vertical shear layer above and below the edge of the disk. Other experiments on barotropic instability have concentrated on the stability of a jet rather than an isolated shear layer. Some experiments have used a thin fluid layer in a parabolic vessel, where the fluid had a free surface and the shear layer was forced by rotating sections of the lower boundary (e.g. Nezlin *et al.* 1990). Cyclonic vortices show a depression of the fluid depth in their centre while anticyclonic vortices have a raised surface. Holton (1971) and Solomon, Holloway & Swinney (1993) used an arrangement of sources and sinks in the base to create a jet. Marcus & Lee (1998) have shown in a theoretical study that for jets the two discontinuities (or strong gradients) of potential vorticity at either side of the jet interact and determine the dynamics, especially observed differences between super-rotating and sub-rotating jets.

The experimental approach in this study follows Niino & Misawa (1984) who forced a circular shear layer in a relatively deep fluid in contact with a rigid lid by rotating sections of the base relative to the rotating tank. This approach avoids topographic effects as well as effects due to surface elevations in the shallow layers described above. All these previous studies have primarily addressed the basic flow structure of the shear layer, its linear stability, and the qualitative global structure of the vortex regime. Detailed studies of the structure and the nonlinear dynamics of the vortices, however, have not been reported previously. A study closely related to barotropic instability by Rabaud & Couder (1983) and Chomaz *et al.* (1988)

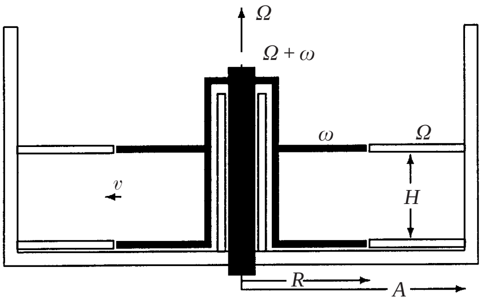

FIGURE 2. Diagram of the apparatus.

investigated flow structures and bifurcations in a circular shear layer in a geometry corresponding exactly to that of Stewartson's problem shown in figure 1, but they chose $\omega > \Omega$, so that neither Coriolis nor centrifugal forces dominated the dynamics, and the dynamics were not that of barotropic instability. Furthermore, the fluid depth was so small that the Ekman layer thickness would be larger than the fluid depth ($E > 1$). The geometrical configuration of our experiment, shown schematically in figure 2, has followed Rabaud & Couder (1983) while choosing parameter ranges similar to Niino & Misawa, such that $E \ll 1$ and typically $\omega \ll \Omega$. The chosen geometry resulted in an up–down symmetry not present in Niino & Misawa's study, and it models very closely the theoretical work by Stewartson (1957).

1.4. *Symmetries and bifurcations*

The important influence of a system's symmetries on the observed flows and their bifurcations has long been known (Ruelle 1973). Our circular tank, with differentially rotating sections of the lid and base as depicted in figure 2 and the resulting basic shear flow have the rotational invariance of the $SO(2)$ group about the rotation axis and the reflection symmetry, Z, about the horizontal mid-plane. The generic bifurcation from $SO(2)$ is to travelling waves (Knobloch 1996) with the C_m symmetry of a wavenumber m, which is a subgroup of $SO(2)$. The baroclinic rotating annulus, e.g. Hide & Mason (1975), is another system which shows the rotational symmetry, but has a more complex vertical symmetry due to the vertical shear of the basic flow. The instability of the basic baroclinic zonal flow is also to travelling waves, consistent with the properties of the $SO(2)$ symmetry group.

With additional symmetries in the system, one of these other symmetries may be broken first in the initial bifurcation while travelling waves may emerge later. An example of this scenario is exhibited by the Taylor–Couette system, e.g. Mullin (1993), which, like the system of this study, has the $SO(2) \times Z$ symmetry. A typical bifurcation sequence in that system is from the axisymmetric and vertically uniform Couette flow to steady Taylor vortices breaking the Z symmetry. This is followed by the emergence of wavy vortices which break the $SO(2)$ symmetry but retain a C_m symmetry.

In the experiment of Rabaud & Couder (1983) and Chomaz *et al.* (1988) with exactly the same symmetries as our system, the initial bifurcation was to travelling waves in the form of steady vortices along the shear layer, in a very similar way to all previous experiments on barotropic instability. The up–down reflectional symmetry was retained throughout most of their regimes, and it was broken only for a very restricted range of parameters in the emergence of a flow pattern like a two-cell Taylor vortex flow. Previous studies of rotating shear layers, e.g. Niino & Misawa

(1984), however, suggest that all observed flows are vertically uniform. Consistent with these observations, theoretical models assume purely two-dimensional flow in the horizontal.

1.5. *Parameters*

The main parameters in this system are the Rossby number and the Ekman number. The Ekman number is a measure of the viscous dissipation compared to the Coriolis term:

$$E \equiv \frac{\nu}{\Omega H^2}. \tag{1.1}$$

While this definition follows the convention adopted by most studies, Hide & Titman (1967) have found that for a spinning disk immersed in a rotating fluid, the radius of the disk rather than the fluid depth should be used for the length scale. Since we have only used two different fluid depths, both having the same order of magnitude as the disk radius, we chose the more common definition.

The Rossby number, Ro, is a measure of the nonlinear advection terms compared to the Coriolis acceleration due to the background rotation of the flow. For a small Rossby number, the nonlinear effects are small, and the dominant balance in the bulk of the fluid is the geostrophic balance, resulting in horizontal, divergence-free flow which may be expressed in terms of a stream function. The Rossby number is defined here as the ratio of the imposed shear velocity (Ro) to the Coriolis term (2Ω) multiplied by a suitable length scale. Two definitions of Ro occur in the literature, which can be distinguished as an external and an internal Rossby number. The external Rossby number uses the fixed length scale of the fluid depth H, while the internal Rossby number uses the thickness of the shear layer L, which depends on the Ekman number as $L = (E/4)^{1/4}H$. In this study the external Rossby number is used:

$$Ro \equiv \frac{R\omega}{2\Omega H}. \tag{1.2}$$

Niino & Misawa (1984) also described the flow by a single parameter, the Reynolds number, defined as

$$Re \equiv \frac{LR\omega}{\nu}, \tag{1.3}$$

where they chose the fluid depth, H, as the scaling length. In the case of a stable Stewartson layer, however, it might be more appropriate to use the thickness of the shear layer, $L = (E/4)^{1/4}H$. In the analysis of the results, it will become apparent that both definition of the Reynolds number are appropriate in different cases. The external Reynolds number, using H, will be denoted by Re,

$$Re \equiv \frac{HR\omega}{\nu} = 2Ro\,E^{-1}, \tag{1.4}$$

and the internal Reynolds number for the $E^{1/4}$-layer will be denoted by Re_i,

$$Re_i \equiv \frac{1}{\sqrt{2}}Ro\,E^{-3/4}. \tag{1.5}$$

With a typical fluid depth of $H = 10\,\text{cm}$, and water as the fluid with a kinematic viscosity of $\nu = 10^{-6}\,\text{m}^2\text{s}^{-1}$, typical ranges of these parameters in the present experiment are $Ro = 0.01$–1.0, $E = 2 \times 10^{-5}$–10^{-3}, and $Re = 10$–10^5 or $Re_i = 1$–2×10^3.

Radius of tank	A	300 ± 3 mm
Radius of disks	R	150 ± 0.5 mm
Fluid depth	H	100 ± 1 mm
Kinematic viscosity	ν (water)	$1.00 \times 10^{-6} \pm 10^{-8}$ m^2 s^{-1}
	(water/glycerol)	$1.66 \times 10^{-6} \pm 10^{-8}$ m^2 s^{-1}
Turntable rotation rate	Ω	0–$+4.0 \pm 10^{-4}$ rad s^{-1}
Disk rotation rate	ω	-0.7–$+0.7 \pm 10^{-5}$ rad s^{-1}
Mean fluid rotation	$\overline{\Omega} = \Omega + \omega/2$	
Rossby number	$Ro = (R\omega)/(2\overline{\Omega}H)$	± 0.01–± 1.0
Ekman number	$E = \nu/(\overline{\Omega}H^2)$	2×10^{-5}–10^{-3}
Reynolds number	$Re = HR\omega/\nu = 2Ro/E$	10–10^5
or	$Re_i = 2^{-1/2} Ro\, E^{-3/4}$	1–2000

TABLE 1. Dimensions of the apparatus, fluid properties, and typical parameters.

2. Experimental apparatus and procedure

2.1. *The apparatus*

The fluid was contained in a cylindrical Perspex tank with a radius of 30 cm as shown in figure 2. In the centre of the tank, a vertical axis of radius 3 cm supported two horizontal circular disks with a radius of 15 cm each (the dark sections in figure 2). Two flat rings were placed in the tank flush with the circular sheets to ensure a uniform fluid depth throughout the domain. The height of the upper disk and ring above the lower surface could be adjusted from 3 to 15 cm but was kept at 10 cm for the experiments presented here. The actual fluid level in the tank was above the upper ring and disk so that the fluid within the test domain was always in contact with the boundaries. The gap between the rotating disks and the stationary rings was about 1mm which was always much less than the width of the inner Stewartson layer; at the smallest obtainable Ekman number, $E = 2 \times 10^{-5}$, the $E^{1/3}$-layer would be 2 mm, and 5 mm at $E = 10^{-4}$. One can therefore expect that only for the smallest achievable values of E the fluid between the disks might be affected by the fluid above the upper disk. The depth of the gap, or the thickness of the disks was 3 mm, as was the fluid depth below the lower disks. The fluid above the upper disks was between > 1 mm and 4 mm with a free surface; these variations were due to the centrifugal effects depending on the background rotation.

The inner axis with the disks was rotated by a stepper motor at angular velocities ω ranging from -0.7 to $+0.7$ rad s^{-1}($\approx \pm 0.1$ Hz). The whole tank was mounted on a steel turntable with a diameter of 1.2 m which rotated anticlockwise at angular velocities of Ω up to 4 rad s^{-1} (≈ 0.7 Hz). These two parameters were controlled by a PC such that either sequences of experiments at fixed parameter values or slow scans of the parameter space by gradually changing one of the parameters or a suitable combination (such as Ro or E) were performed. In the latter case, a typical scan would cover a range of one or two orders of magnitude in Ro or E in ten hours. Table 1 summarizes the physical dimensions of the apparatus, together with the fluid properties and the principal dimensionless parameters.

Two complementary ways to monitor the flow were used: laser-Doppler velocimetry (LDV) to obtain high-precision time series, and particle tracking (also known as particle image velocimetry, PIV) to obtain snapshots of the global horizontal flow field. Owing to the different densities of the seeding particles, different fluids had to be used, namely water for the LDV measurements and a water–glycerol mixture for the particle tracking experiments.

Using LDV measurements, the radial velocity at a single point in the shear layer was measured with a forward-scattering LDV system from TSI which was mounted on the turntable. The measurement point was at mid-height in the centre of the shear layer fixed in the frame of the tank. The working fluid was water, seeded with 6 μm latex beads to give a consistent Doppler signal. The laser was a 10 mW red He/Ne laser, with one of the beams frequency-shifted by 20 kHz. The Doppler signal was analysed with a TSI IFA-550 with an analogue output card linked to a PC. It was found that a sampling rate of 1 Hz, each sample calculated as the average over 100 measurements, was appropriate for all investigated flow types. Large jumps in the raw time series were an artefact of the LDV processing and were replaced by the average of the previous and successive data point. The velocity range for all experiments was from -30 to $+60\,\mathrm{mm\,s^{-1}}$, where a typical vortex flow had maximum velocities of about $\pm 10\,\mathrm{mm\,s^{-1}}$ with a measurement accuracy about $\pm 0.2\,\mathrm{mm\,s^{-1}}$.

The horizontal velocity field at mid-height was obtained by recording neutrally buoyant tracer particles with a CCD video camera mounted on the turntable viewing the tank from the top. The tracer particles were pliolite beads with a diameter of 600 to 700 μm, and the working fluid was adjusted to have the same density as the particles, $\rho = 1044$ kg m^{-3}, by adding glycerol to water which resulted in a kinematic viscosity of $\nu = 1.66 \times 10^{-6}$ m^2 s^{-1}. The particles were illuminated by a horizontal light sheet with a thickness of around 5 mm produced by three light sources each consisting of a projector lamp and a cylindrical lens. Owing to refraction of the light on the cylindrical sidewall of the tank, the illumination was not uniform throughout the tank, and three areas near the outer perimeter were darker. The images, recorded onto S-VHS tapes, were nevertheless of sufficient quality to construct global flow fields using the software package *DigImage*, developed at Cambridge (e.g. Dalziel 1992). Each velocity field is calculated from 16 video frames, each 0.4 s apart, resulting in a flow field averaged over 6 s.

2.2. *Procedure and data analysis*

To cover the parameter space defined by the Rossby and Ekman numbers efficiently, one of these parameters was slowly scanned over the range of the apparatus and the other was kept constant while the flow regimes were recorded. After the parameter space was covered, experiments at fixed parameter values were performed to obtain long time series of the flow, using LDV, and to obtain snapshots of the global horizontal flow field using *DigImage*.

2.2.1. *Time-dependent forcing*

When the regime diagram was scanned by slowly varying one parameter, the main interest was in determining the qualitative behaviour and the nature and location of transitions and bifurcations. Bifurcation diagrams were most efficiently constructed from velocity time series using the LDV system. Since the axes on the regime diagram are logarithmic, the rate of change of the bifurcation parameter was chosen to be logarithmic in time. Therefore, a time series of the measured velocity plotted on a linear time axis corresponds to a bifurcation diagram traversing the logarithmic regime diagram at a constant rate. Each scan of a parameter lasted typically 7–12 hours, where no discernible difference in the observed flow types and transitions was found between different rates of change. Both directions, increasing and decreasing the parameter, were employed since hysteresis is known to be a common phenomenon in fluid experiments and was observed in the present system.

Besides using the time series of the radial velocity as a bifurcation diagram, it was found that tracing the time evolution of the independent frequencies within short windows of the series was an efficient method of tracking mode transitions and bifurcations such as period-doubling bifurcations. To do this, spectrograms were obtained by calculating a time series of FFT power spectra over a short window (typically 1024 s), from which the dominant maxima were found. Higher harmonics of an identified maximum, as well as sum or difference frequencies, were discarded, but subharmonics could be retained to detect period-doubling bifurcations. The independent frequencies, normalized by half the differential rotation – the winding number, $W \equiv 2\pi f(\omega/2)^{-1}$ were then plotted as functions of the bifurcation parameter. If the flow structures were to move at the mean velocity of the shear layer then they would move in the reference frame of the outer section at half the velocity of the inner section. The value of W for a single structure swept around the tank would then be equal to one, and a structure with an azimuthal wavenumber m would correspondingly have $W = m$. The variations of the winding number showed mode transitions very clearly, and it was possible to infer the number of vortices from these frequencies, though the observed values of W were not restricted to integers. The relationship between the dominant frequency and the wavenumber was confirmed in the flow visualization experiments.

The power spectral amplitude at the dominant frequency was used to characterize some of the observed bifurcations. Using a suitable normalization, the amplitude is a measure of the amplitude of the dominant oscillation which can be used to construct a traditional bifurcation diagram. The conversion from power spectral amplitude to a normalized velocity amplitude used here is defined as the square root of the power spectral density normalized by the imposed shear velocity.

2.2.2. *Steady forcing*

Once the regime diagram was mapped out, longer time series under constant forcing were obtained to examine the dynamics and temporal statistics of the individual regimes. The experiments were performed in a number of stages. After spin-up from rest to an initial point in parameter space, the flow was allowed to settle for 30 min before data were taken for a period of 4 hours. Then either the Rossby number or the Ekman number was changed smoothly over 30 min while the other parameter was held constant. Following the change in parameters, the flow was again left for 30 min before another set of velocity data was taken for a further period of 4 hours. This procedure was usually continued until the physical limitations of the apparatus were reached, or until the flow became axisymmetric (depending on the direction of the change in E or Ro). This procedure was applied to both modes of operation, LDV and particle tracking. Owing to the limitation of 3-hour video tapes, the time scales for the particle tracking were much shorter, 5 minutes for changing the parameter and equilibration and 10 minutes for recording the flow. Before the tape was started, the flow was allowed to settle into an equilibrium state for at least 30 min.

LDV data obtained in this way were analysed with linear techniques, such as power spectra, as well as Singular Systems Analysis (SSA). To obtain information on the statistical significance of features in the power spectrum, the average of several power spectra from subsets of the time series was used. When the low frequencies were more interesting than the high-frequency components, the subsets were constructed from interlaced, sub-sampled series. For example, for an average of m spectra, only every mth measurement was taken. Possible aliasing effects introduced by the sub-sampling were tested by obtaining average spectra from different sub-sampling rates. This procedure showed that aliasing could result in strong spectral peaks, but that these peaks were easily identified. Useful averaged spectra from up to about ten individual spectra were obtained. For averaged spectra of higher frequencies, short sections of the time series (typically 1024 points) were used.

SSA provides information on the qualitative dynamics of the flow by reconstructing the phase portrait using the singular value decomposition (SVD) of a time-delay covariance matrix of the radial velocity time series (Broomhead & King 1986). This procedure ensures that the dynamics of the flow with the strongest variance is described by a small number of singular vectors. This technique is much less sensitive to the correct choice of the delay time or the window length. Best results, however, are obtained if the window length is comparable to, or larger than, the main period of the oscillations. When low-dimensional dynamics are contaminated with white noise, then the leading singular vectors span a sub-space of the phase space which is an embedding of the low-dimensional attractor, while the remaining singular vectors are dominated by the uncorrelated noise. The orientation of the significant singular vectors is such that the signal-to-noise ratio is maximized. The projection of the delay time series onto M leading singular vectors gives the trajectory in an M-dimensional embedding which can be used to construct phase portraits, Poincaré sections, return maps, and to estimate the attractor dimension (using the algorithm from Grassberger & Procaccia 1983) and the largest Lyapunov exponent (Wolf *et al.* 1985).

By finding the eigenvectors of the covariance matrix, SSA effectively separates dynamic signals from *white*, uncorrelated noise. Frequently, the signal of interest is not only contaminated by white noise but also by coloured noise, or it may be masked by a strong known signal. A variant of SSA, called here *reference SSA* or R-SSA, was designed by Allen & Smith (1997) to extract dynamic information from a time series contaminated by a known or estimated noise process. The procedure is to find a coordinate transformation for the covariance matrix of the data series such that the contaminating noise or signal becomes uncorrelated. This coordinate transformation is provided by the SSA analysis of a time series which only contains the ‘contamination’. For instance, to detect a weak modulation of a strong oscillation, the oscillation which is masking the modulation has to be treated as the contamination. SSA analysis of a time series from an unmodulated oscillation provides the eigenvectors for this flow and with it the transformation matrix to ‘filter out’ the strong oscillation. Components of the transformed time series which are not consistent with the ‘contamination’ time series (the modulation in the example) will be picked out in the singular value decomposition as eigenvectors with eigenvalues above a calculated noise floor. In the following, the notation to indicate which flow regime containing the unwanted signal was used to find additional information in a time series is A/B, where A is the time series containing the unknown signal contaminated by ‘noise’ described by B.

3. The regime diagram

This section presents an overview of the flow regimes found in the experiments. The two regime diagrams for a parameter space defined by the Rossby and Ekman numbers, shown in figures 3 and 4 for positive and negative Ro respectively, were derived mainly from the experiments with the ramped forcing. The structure of the regime diagrams was then confirmed and refined by the subsequent experiments

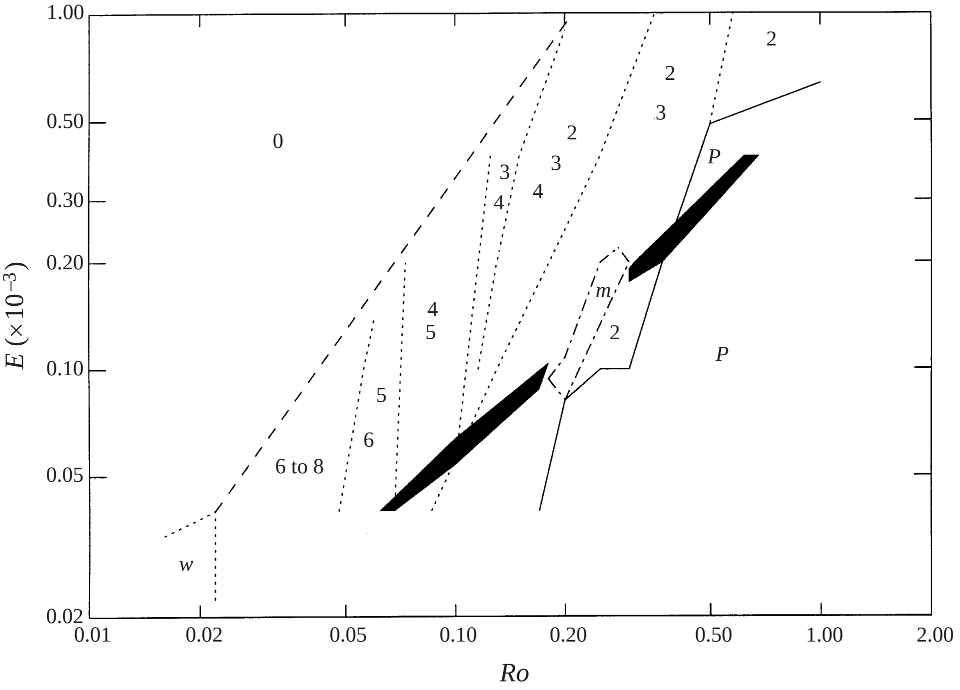

FIGURE 3. Regime diagram for positive Ro obtained from experiments using the method from § 2.2.1. The black areas denote highly irregular flow (I), 0 the stable basic flow, m modulated oscillations, w weak fluctuations about zero velocity, and P period-doubled solutions. The numbers refer to the wavenumber of the vortex flows. Solid lines denote transitions without any noticeable hysteresis, and broken lines denote hysteretic transitions. The region of modulated oscillations is indicated by a dash-dotted line.

with steady forcing. When the inner disks rotate with the same orientation as the background rotation then the Rossby number is defined to be positive, otherwise to be negative.

The axisymmetric solution and the regime of relatively regular vortex flows with different numbers of vortices are indicated by 0 and wavenumbers, m, respectively. One phenomenon observed in common with all shear layer experiments mentioned in § 1.2 is the successive transition to lower numbers of vortices as the supercriticality (with respect to the initial instability) is increased – either by increasing $|Ro|$ or $|Re|$ or by decreasing E. Reversing the change in the parameter resulted in a corresponding increase of the vortex number, though substantial hysteresis was observed. This hysteresis is shown by the dotted lines and the multiple numbers in the regime diagrams. For example, at $(Ro, E) = (-0.08, 1.5 \times 10^{-4})$ one would observe six vortices if one approached the point from the left (small Ro) or top (large E), but four vortices on approach from the right (large Ro) and five vortices when starting from below at small E.

Figure 5 shows a time series of the radial velocity or bifurcation diagram as $|Ro|$ was gradually increased, while E was kept fixed at $E = 10^{-4}$. This time series is divided into four panels, where the beginning is at the top left. The second panel continues from the end of the first, and so on, to the end of the time series at the bottom right. The first impression is that the initial flow is a zero solution, occasionally perturbed by bursts of activity. This is followed by oscillations, sometimes regular, sometimes

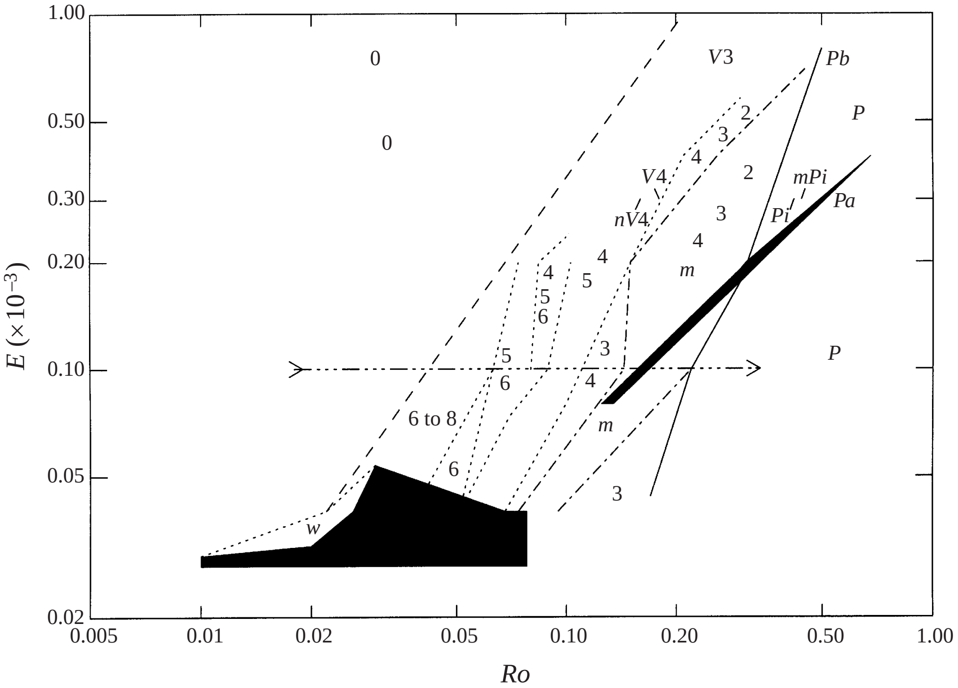

FIGURE 4. Regime diagram for negative *Ro*. This diagram also indicates the locations of the individually discussed examples and the line traversed by the scan shown in figure 5. Since *nV*4 and *V*4, and *Pi* and *mPi* are very close, they have been moved apart and the lines point to the actual position. The other labels, 0, *V*3, *Pa* and *Pb* are printed at their respective parameter values. The labels are described in § 5.

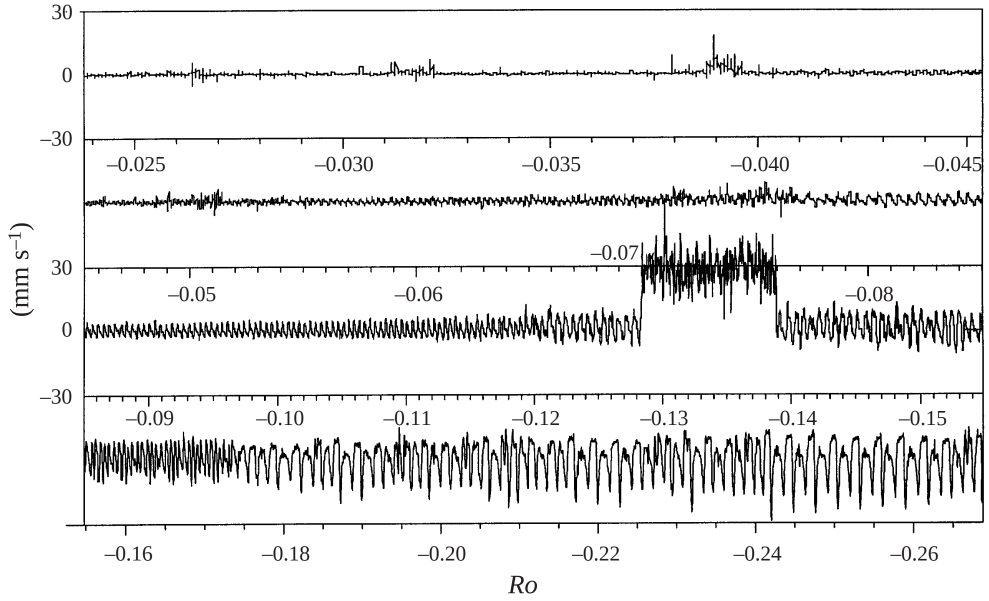

FIGURE 5. Time series or bifurcation diagram at $E = 10^{-4}$ for negative *Ro*, increasing in magnitude. The time series begins at the left of the top panel, and is continued in the following panels.

with strong noise added. More complex flows appear at relatively large values of $|Ro|$, namely modulated flows, aperiodic oscillations, and highly irregular flows.

The axisymmetric, or zero, solution is that of the stable Stewartson layers which become unstable to travelling waves at a critical Rossby or Ekman number. The observed bursts in the axisymmetric regime could be an indication that the shear layer might be weakly unstable (possibly convectively unstable) before the visible onset of relatively regular oscillations. These oscillations are clearly distinguishable above $|Ro| = 0.051$, but might be present before though hidden in the measurement noise. Other indications of weak instabilities are found at very small values of Ro and E. There, the velocity measurements were characterized by weak, irregular fluctuations around zero velocity. The transition to regular oscillations, which also appears to be accompanied by a burst of a strongly noisy signal will be discussed in detail in the following section, § 4. The oscillation which is visible beyond $Ro = -0.051$, shows a further period of perturbed flow around $Ro = -0.075$. These perturbations are followed by a marked increase of the oscillation period. This increase of the period reflects a mode transition to a lower wavenumber which will be discussed in § 5.

3.1. *Irregular flow solutions*

The highly irregular flow for $0.129 < -Ro < 0.139$ is not an artefact of the LDV system, but is a repeatable feature of the experiment, occurring over a well defined range of parameters with only little hysteresis. This irregular flow, indicated by the black areas in figures 3 and 4, occupies a substantial part of the regime diagrams. For positive Ro, the regimes appear as a two narrow strips aligned at a line of constant Ro/E. This would indicate that the Reynolds number, as defined by the external dimension in (1.4), determines the occurrence of this irregular flow. The Reynolds number at which the transition to this flow is found is $Re = 2550$, and the transition back to predominantly horizontal motion is at $Re = 2800$. This range also applies to one of the irregular regimes found at negative Ro.

The other irregular regime, for small E at negative Ro, has a different velocity structure with fluctuations around much smaller velocities than any of the other irregular regimes and appears to be a different flow regime, possibly linked to the weak fluctuations indicated by w in figure 4. It is possible that this flow may be affected by the gap between the split disks and the fluid above the upper boundary layer, because at these values of E, the $E^{1/3}$ layer is not very much thicker than the gap.

As apparent in the time series in figure 5, the flow in the irregular regimes at positive Ro and the upper irregular regime at negative Ro is characterized by strong fluctuations around a positive mean velocity, where the velocity generally remains positive. The positive velocity almost certainly implies that the flow is fully three-dimensional in this regime. This conclusion is drawn from the fact that the measurement point of the LDV system is in the frame of the outer tank in which the mean shear layer rotates at approximately $\omega/2$. If the flow is always positive at the measurement point, it follows that it will also be positive at all other points in the fluid with the same radius and height. Mass continuity then requires substantial negative velocities above or below mid-height. It is possible that the flow structure may be similar to that of a two-vortex state found in the Taylor–Couette system.

A flow of two vertically stacked convection cells was observed in the circular shear layer experiment by Rabaud & Couder (1983) which would be consistent with our LDV signal. They observed this flow for large Reynolds numbers (though still an order of magnitude smaller than observed here) in a relatively deep fluid ($0.3 \leqslant H/R \leqslant 0.6$).

Their suggestion that this flow arises from a centrifugal instability, however, cannot be transferred to our observations, since we observed the irregular flow not only for positive but also for negative ω, where the centrifugal force increases outwards and inhibits centrifugal instability. While some preliminary visualizations of a vertical section have indicated the existence of Taylor–like cells, their structure and dynamics are not yet understood.

3.2. *Modulated vortices*

At $Ro = -0.139$ in the time series in figure 5, the flow appears to switch back to the vortices observed before the onset of the irregular flow. These vortices then develop a modulation with a period of 4–5 times of that of the vortex drift, denoted by m in the regime diagrams in figures 3 and 4. From the LDV measurements alone, it is not possible to determine the exact nature of these flows, for instance if they are a temporal modulation of a single wave mode $m = 3$ or if they are a spatial modulation due to an interference of two dispersive wave modes. This flow regime is analysed in detail in Part 2 using LDV and particle tracking experiments. From the regime diagram, the modulated regime appears to be linked in some way to the irregular regimes, where the modulated regimes forms regular 'islands' between and around the two irregular regimes for each sign of the Rossby number.

The final distinct flow change in the time series in figure 5 is another mode transition leading to a flow with a relatively low frequency. This flow shows clear evidence of a period-doubled signal towards the end of the time series. These regimes, which show a period-2 flow, or a more complex flow with a strong period-2 component, are denoted with P in the regime diagrams in figures 3 and 4, and are discussed further in § 5.4.

4. The axisymmetric flow and its instability

4.1. *The axisymmetric flow*

The horizontal velocity of the stable axisymmetric flow is shown in figure 6 together with the mean azimuthal velocity and the radial shear of the azimuthal velocity. Even at these parameter values, $Ro = -0.035$ and $E = 3 \times 10^{-4}$, the velocity from the particle tracking showed some deviation from rotational symmetry which may be caused by the fitting of the velocities onto a rectangular grid. If the width of the shear layer is defined as the half-width of the peak in figure 6(*c*), then the shear layer thickness is approximately 40 mm. With an Ekman number of $E = 3 \times 10^{-4}$, the thickness of the outer Stewartson layer would be $\delta = 9.3$ mm, which is about a quarter of the measured thickness but, given the spatial resolution of the particle tracking set-up, those values are not inconsistent with each other. Owing to these limitations of the particle tracking experiments, it is not possible or feasible to follow the scaling of the shear layer thickness over a large range of E, but Baker (1967) measured the profile of the axisymmetric flow in a similar geometry. While he also observed that the shear layer tended to be thicker than predicted, the thickness was found to scale with $E^{1/4}$ (a variant of the derivation is presented in Greenspan 1968, § 2.18).

4.2. *Linear stability*

To examine the linear stability of the basic shear flow, Greenspan (1968) separated the fluid into Ekman layers and the inviscid interior. The equations were expanded in powers of $E^{1/2}$, and then a stability criterion in the form of Rayleigh's inflection-point criterion was obtained. This approach, however, neglected viscous effects in

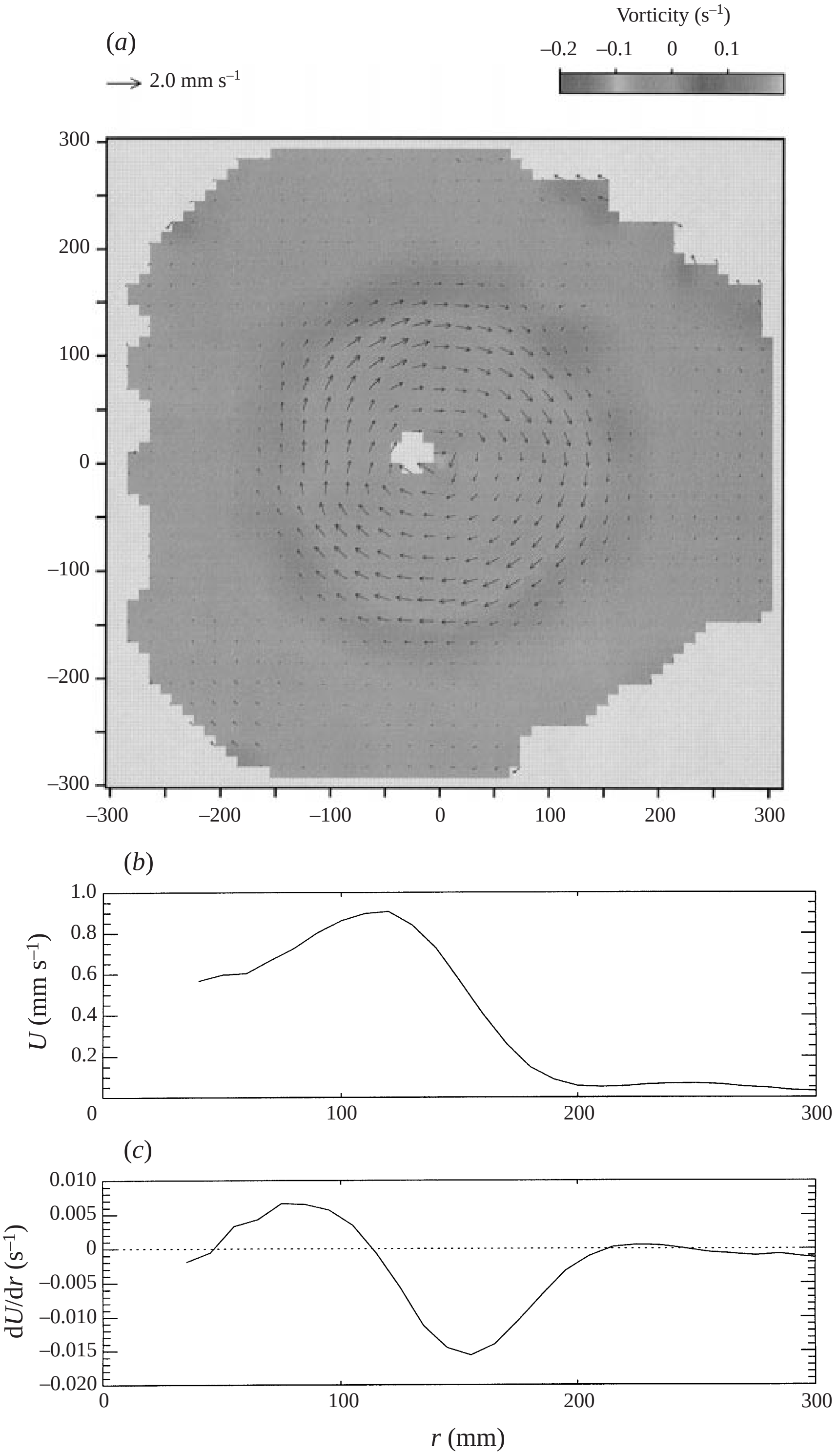

FIGURE 6. The flow field of the axisymmetric flow: (*a*) the velocity field is indicated by the arrows and the vorticity map by the grey scale; (*b*) the radial profile of the mean azimuthal velocity, and (*c*) its radial shear.

the Stewartson layers. A typical boundary layer approach to include the effects of viscosity in the Stewartson layer was presented by Hashimoto (1976) where the fluid region is divided into an inviscid interior and viscous boundary and shear layers using the scaling of the Ekman layers and the two Stewartson layers. The resulting instability criterion implied that an infinite set of unstable wavenumbers exists for every combination of Ro and E. The lack of a short-wave cut-off, however, is in contradiction with previous experimental observations.

Niino & Misawa (1984) noted that Hashimoto had neglected some of the terms related to the streamwise gradient of vorticity. They proposed a different approach which included explicit dissipation in the fluid interior. To make progress they used the quasi-geostrophic approximation, which cannot resolve the $E^{1/3}$ layer. According to Greenspan, the contribution to the tangential velocity from the $E^{1/3}$ layer vanishes when averaged over depth, and it is therefore assumed to have a small effect on the barotropic instability. The principal stability parameter is the internal Reynolds number as defined in (1.5). This would suggest that the instability is primarily a shear instability, where the influence of the background rotation is restricted to the fact that the shear is concentrated in a boundary layer of thickness $E^{1/4}$. In addition, the curvature of the circular shear layer has a small influence on the stability. The ratio of the radius of curvature of the shear layer to the shear layer thickness, $\gamma = R/\left((E/4)^{1/4}H\right)^{-1}$ modifies $Re_{i,c}$ and the most unstable wavenumber. For $\gamma \rightarrow \infty$ ($\gamma \gtrsim 30$), the first wave to become unstable at $Re_c = 11.6$ has a wave vector of $k = 0.28$, which increases to $k = 0.5$ and $Re_c = 20$ at $\gamma = 3$. The effect of the curvature of the shear layer is therefore to stabilize the layer and to shift the unstable modes to shorter waves.

The range of γ covered in the present experiment is from $\gamma = 12$ at $E = 10^{-3}$ to $\gamma = 32$ at $E = 2 \times 10^{-5}$. Therefore, at $E = 2 \times 10^{-5}$ we would expect $k \approx 0.28$ which corresponds to a wavenumber of $m = k\gamma$ of 8, and at $E = 10^{-3}$ we would expect $k \approx 0.31$ or $m = 3$.

4.3. *The bifurcation to vortices*

As the Ekman number was reduced or the Rossby number increased, low-frequency fluctuations began to emerge in the time series, which became stronger and more coherent with the gradual strengthening of a particular frequency range until a definite vortex structure was established. Purely from the time series in figure 5 it is not possible to decide if the boundary layer theory is correct where the higher modes cannot be distinguished from measurement noise, or if there is a short-wave cut-off, and with it a critical parameter, for the onset of vortex solutions. If the short-wave cut-off exists, as predicted by the quasi-geostrophic theory, then the onset of oscillations could be through a supercritical Hopf bifurcation, because the oscillation frequency is constant near the onset (see below in § 5.2, figure 12*a*) and the amplitude appears to grow gradually. For a supercritical Hopf bifurcation, the amplitude of the vortices would go to zero at a well defined parameter value. On the other hand, for a continued existence of the vortices below the noise level, one would not expect to be able to extrapolate the amplitude to zero at a finite parameter value.

If the emergence of the vortices is consistent with a supercritical Hopf bifurcation, the amplitude of the oscillation grows with the square root of the bifurcation parameter. To show the amplitude behaviour more clearly, the square of a measure of the amplitude is plotted in figure 7(*a*), namely the power spectral density at the dominant oscillation frequency normalized by the velocity of the disks in the shear layer. Since for small Ro this normalization involves the division of two small numbers contami-

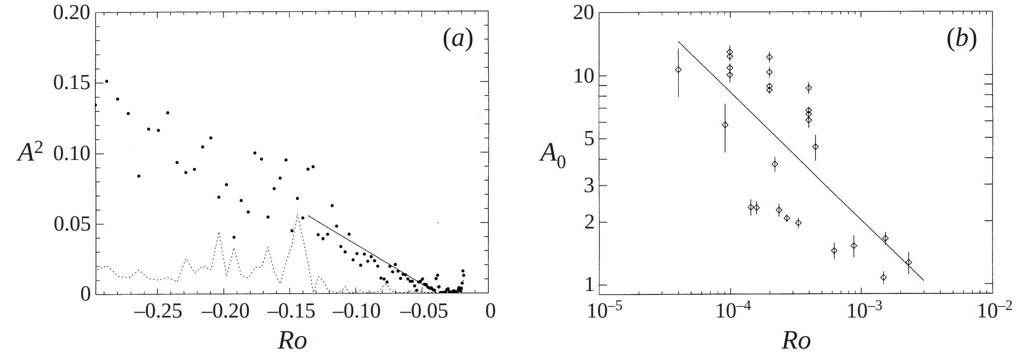

FIGURE 7. (*a*) Plot of non-dimensionalized amplitudes corresponding to the two strongest independent frequencies against the Rossby number at $E = 10^{-4}$ of the time series shown in figure 5. The black dots are the amplitude of the dominant frequency, and the dashed line that of the second independent frequency. The solid line is a line fitted to the dots in the interval $0.04 < |Ro| < 0.14$. (*b*) The scaled amplitude of the fitted Hopf bifurcation as a function of the Ekman number.

nated by noise, the noise is strongly amplified. Nevertheless, it is possible to see that the squared amplitude increases linearly above a critical value of *Ro*. The dashed line shows the amplitude of oscillations at the second independent frequency. At a point where more than one oscillation is strong the flow is strongly nonlinear and the local unfolding of the Hopf bifurcation is no longer valid. This point is clearly reached at $-Ro = 0.1$ which corresponds to the irregular regime followed by the modulated flow. Therefore only the section below the irregular regime was used for the line fitting which resulted in

$$v = A_0 \, |Ro - Ro_c|^{1/2} \tag{4.1}$$

with $A_0 = 0.75 \pm 0.03$ and $Ro_c = -0.039 \pm 0.003$ for $E = 10^{-4}$. As expected, this extrapolation goes below the visible onset of oscillation at $|Ro| = 0.051$, and the onset of oscillations is extrapolated to $Ro_c = -0.039$ which coincides with one of the bursts of fluctuations in the time series in figure 5.

Most importantly, the finite value for the onset of vortex flows and a square-root dependence of the vortex strength indicate that the onset of vortex solutions in the rotating shear layer is through a supercritical Hopf bifurcation. This implies the existence of a short-wave cut-off, which is absent in the boundary layer theories, but provided in the quasi-geostrophic theory by dissipation in the fluid interior (outside the shear layers).

4.4. *The instability criterion*

Figure 8 shows the experimentally determined points of marginal stability where the error bars were derived from the curve fitting procedure used for (4.1). Even though the points in the figure are compiled from both positive and negative *Ro*, and from changing either parameter in either direction, the general shape of the stability curve is almost a straight line. No difference for the different directions of the relative rotation is apparent. The critical Rossby number, Ro_c, varies with E as

$$Ro_c = 27(\pm 1)E^{0.72 \pm 0.03} \tag{4.2}$$

with a correlation coefficient of $r^2 = 0.94$, as indicated by the solid line in figure 8. While the scaling exponent differs from that deduced by Hide & Titman (1967) (who obtained $Ro_c = 29E^{0.6}$), it agrees qualitatively very well with the theoretical prediction

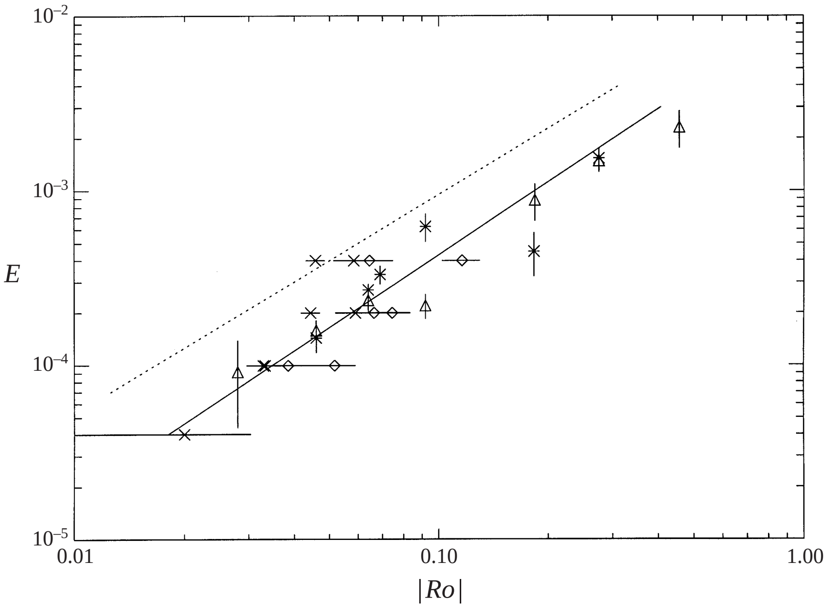

FIGURE 8. Instability of axisymmetric flow. The × and stars denote experiments with positive *Ro*, and diamonds and triangles denote negative *Ro*. The solid line is a best fit of a power law scaling to the data, and the dotted line is the linear instability calculation from Niino & Misawa (1984).

of Niino & Misawa (1984) which is shown in figure 8 by the dotted line although it is shifted to larger values of *Ro*. The implication is that the onset of instability can be described by the internal Reynolds number, where the critical value is weakly dependent on *E*. Using (4.2) and the definition of the internal Reynolds number in (1.5), one obtains for the critical Reynolds number

$$Re_{i,c} = 19E^{-0.03} \approx 24 \pm 2. \tag{4.3}$$

Since the instability seems to be determined by an Ekman-number-dependent Reynolds number, it was suggested that the amplidude of the Hopf bifurcation, i.e. the gradient in figure 7(*a*) or A_0 in (4.1), might also be described as a function of the Ekman number. Since the magnitude of the gradient from the linear regression varied dependent on whether *Ro* or *E* was the bifurcation parameter, the two sets were initially investigated separately, that is, all experiments for both signs of *Ro* and either direction of change of the bifurcation parameter were correlated which resulted in two independent correlations for the amplitude of the Hopf bifurcation. With *Ro* as the parameter, we obtained $A_0 = 4.3Ro^{-0.35}$, and with *E* the correlation was $A_0 = 0.075E^{-0.26}$. To test if these two results could be combined to a single description of the amplitude, the amplitudes were scaled by their respective constant, i.e. 4.3 for changing Rossby number and 0.075 for varying Ekman number. The A_0 scaled in this way are shown as a function of *E* in figure 7(*b*) together with a regression analysis which resulted in

$$A_0 = A_{00}E^{\alpha} \tag{4.4}$$

with $A_{00} = 0.030 \pm 0.005$ and $\alpha = -0.6 \pm 0.1$ with a correlation coefficient of $r^2 = 0.7$. While the correlation is not very large, the two sets of results from either *Ro* or *E* as the parameter are not distinguishable in the combined set.

Label (rad s^{-1})	Ω (rad s^{-1})	ω (rad s^{-1})	Ro	E ($\times 10^{-3}$)	m	$W_{1,2}$	Figure nos.
	0.172	−0.011	−0.035	0.73	0	—	6
$V3$	0.216	−0.100	−0.25	0.73	3	—	9
$V4$	0.267	−0.068	−0.18	0.30	4	2.49	10, 11, 15
$nV4$	0.263	−0.061	−0.16	0.30	4	2.49	13, 14, 15, 16
Pa	0.332	−0.198	−0.53	0.30	1/2	0.50	17, 18
Pb	0.266	−0.199	−0.50	0.73	1/2	—	19, 21
Pi	0.311	−0.157	−0.42	0.30	1/2	0.56	20, 22
mPi	0.315	−0.164	−0.44	0.30	1/2	2.05, 0.55	20, 22, 23

TABLE 2. Specific cases discussed in § 5.

The critical Rossby number decreases as E decreases. This is not surprising since, as E decreases, the thickness of the shear layer becomes smaller, and the shear becomes more concentrated. As a result, the local velocity shear increases for any given total radial shear as measured by Ro, and the layer becomes unstable earlier. This is also represented in the internal Reynolds number which scales the velocity shear with the Stewartson layer thickness. The Reynolds number, however, cannot capture the wavenumber of the most unstable mode, but it can be described by the layer thickness. As the thickness of the shear layer decreases, the radial length scale and with it the size of the vortices also decrease coupled with an increase in the number of vortices. The invariance of the instability criterion with respect to the sign of the Rossby number supports further the validity of the quasi-geostrophic approximation which also has this invariance.

5. Vortices

In this section, the characteristics of steady vortices will be presented. The typical cases discussed here are listed in table 2. In the text they will be referred to by a label indicating the flow regime they were selected from, namely V for regular vortices, nV for noisy vortices, and P for period-doubled vortices. When referring to these specific experiments, their respective label, e.g. $V3$, will be used in the text and figure captions. The labels also indicate these experiments in the regime diagrams in figures 3 and 4.

5.1. *Regular vortices*

A typical vortex flow is shown in figure 9, $V3$ at $Ro = -0.25$ and $E = 7.3 \times 10^{-4}$. The shear layer is deformed into a wavy pattern with three troughs and ridges and three counter-rotating vortices on the outside of the shear layer. This entire flow pattern rotates as a steady pattern in the tank at somewhat less than half the inner disk rotation. A short segment of the LDV time series of the radial velocity from $V4$, an $m = 4$ flow, is shown in figure 10(a). The dominant feature of the time series is the large oscillations which correspond to the drift of the troughs and ridges past the measurement point. Some weaker fluctuations can be seen which could be due to noise or a weak modulation of the flow field. The power spectrum of the time series, in figure 10(b), shows very distinctly the main frequency of $f_1 = 1.354 \times 10^{-2}$ Hz ($T = 73.8$ s) of the wave drift. The higher harmonics of the main frequency are due to the non-sinusoidal shape of the oscillation. The spectrum was obtained from the average of ten sub-sampled spectra, and the two dotted lines indicate the level of

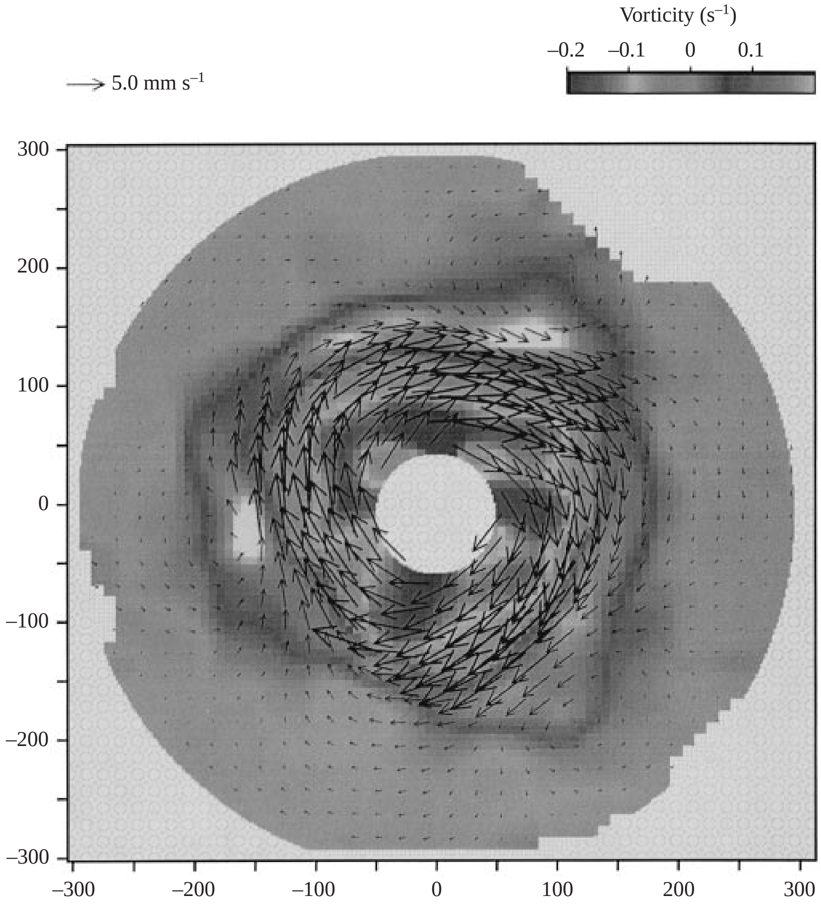

FIGURE 9. Velocity field and vorticity map of $V3$, an $m = 3$ flow with three vortices at the outer edge of the shear layer ($Ro = -0.25$, $E = 7.3 \times 10^{-4}$).

statistical significance. The lower line is one standard deviation (s.d.) above the mean power, and the second is 2 s.d. above the mean. The mean was here calculated from 80% of the spectrum where the strongest components were omitted to eliminate the obvious frequencies from the vortex drift. Rejecting any frequency component with less than 2 s.d. above the mean still leaves a peak at $f_2 = 1.028 \times 10^{-2}$ Hz, together with peaks at combinations of f_1 and f_2, as a significant modulation of the flow.

A phase space reconstruction for the periodic flows using SSA resulted in a broadened limit cycle. The example shown in figure 11(a), which was obtained from the $m = 4$ flow shown in figure 10, used a window length of 80 s to cover a complete cycle of the vortex drift. The Poincaré section at the zero crossing of the first principal component showed two well defined regions, but without any obvious internal structure. The first return map (of the second principal component at positive crossings of the section in figure 11b), however, indicates that the points are arranged on a very ‘fuzzy’ toroidal structure around a clear centre. This is further support for the presence of modulation of the vortex flow as indicated by the power spectrum. Its Grassberger–Procaccia dimension estimates showed a small but distinct scaling region with a correlation dimension of between $d_c = 1.2$ and 1.8 for embedding dimensions between 5 and 9 as shown in figure 11(d) confirming the presence of

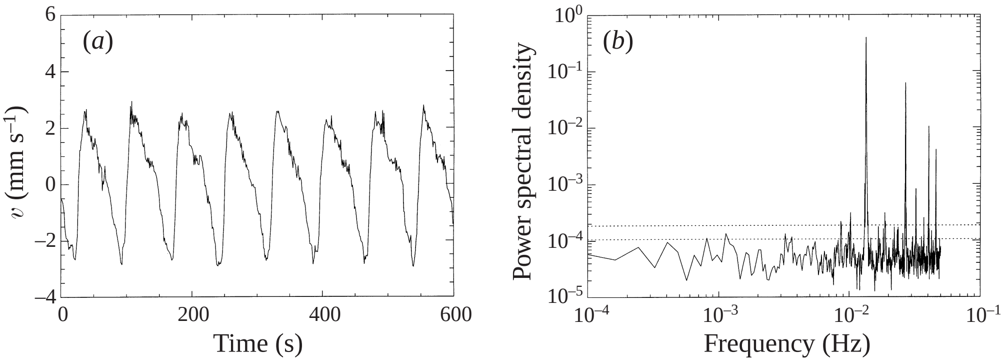

FIGURE 10. (*a*) Short segment of a times series of radial velocity, and (*b*) power spectrum for periodic vortices ($V4$).

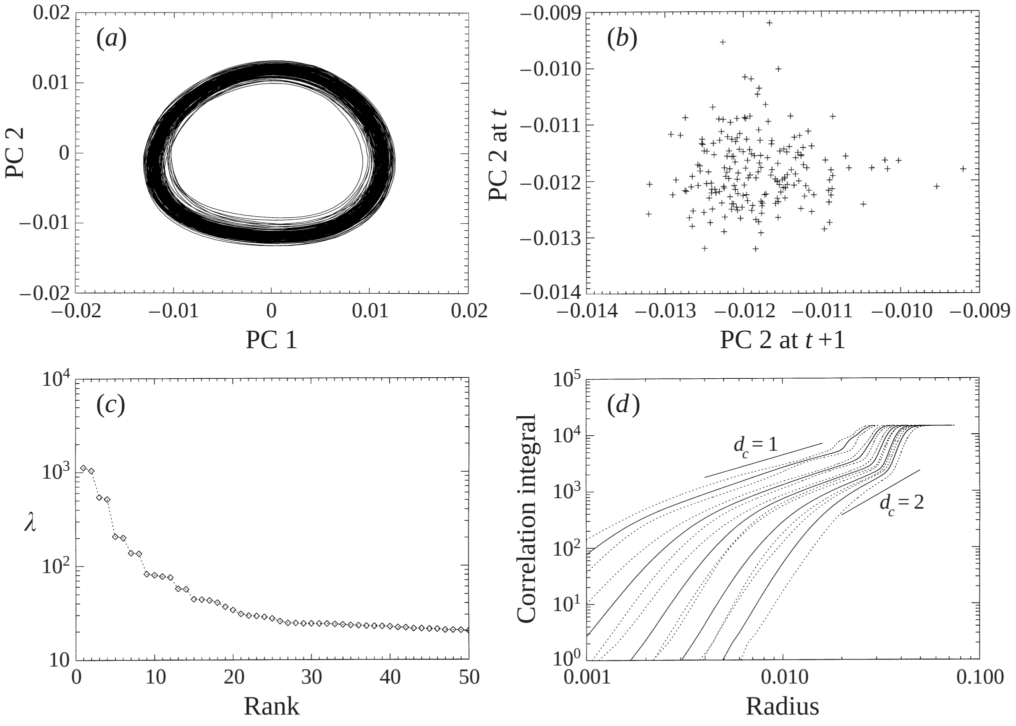

FIGURE 11. Phase space reconstruction for the regular vortex flow $V4$ using SSA. (*a*) Phase portrait and (*b*) first return map of the second principal component at the positive crossing of the Poincaré section where the first principal component is zero for a regular vortex flow (V); (*c*) Eigenvalues of the singular value decomposition, and (*d*) correlation integral for embedding dimensions 3, 5, 7, 9, and 11, together with indication of the scaling limits.

chaotic low-dimensional chaos. With embedding dimensions larger than about 10, the noise component becomes too strong for the algorithm. A dimension of approximately 1.5, however, is not consistent with that arising from an instability of a torus which would result in a fractal dimension $d_c > 2$. This contradiction suggests that one should interpret the result with caution.

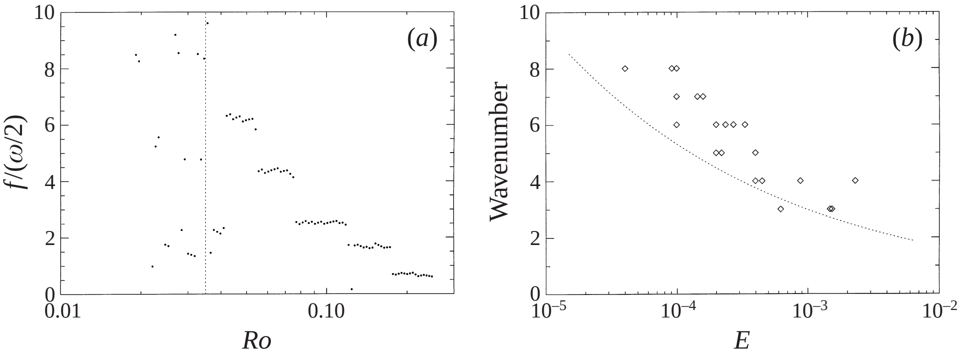

FIGURE 12. (*a*) Plot of the strongest frequency against the changing parameter $-Ro$ at $E = 10^{-4}$ of the time series shown in figure 5. (*b*) The wavenumber found at the onset of vortex flows against the Ekman number. The dotted line indicates the most unstable wavenumber after Niino & Misawa (1984).

5.2. *Dispersion relation*

The transitions between wavenumbers are most clearly seen in a plot of the winding number against the varying parameter. An example of this is shown in figure 12(*a*) for the time series shown in figure 5. The location of the critical Rossby number found in (4.1) is marked by a vertical dashed line. Distinct sections of virtually constant winding number can be seen. Jumps in W_1, e.g. at $Ro = -0.051$ from $W_1 = 6.3$ to 4.4 and at $Ro = -0.075$ to $W_1 = 2.5$, correspond to mode transitions to lower vortex numbers. Flow visualization experiments revealed that $W_1 \approx 0.7$ corresponds to a mode $m = 2$ and $W_1 \approx 1.6$ to $m = 3$, and so on. Linear relationships for each sign of Ro between the winding number and wavenumber were fitted separately but gave the same results within the calculated error margins,

$$m = 1.2(\pm 0.2) + 1.12(\pm 0.06) W_1 \tag{5.1}$$

with a correlation coefficient of $r^2 = 0.997$ for $Ro > 0$ and $r^2 = 0.989$ for $Ro < 0$. Using this correspondence, figure 12(*a*) can be interpreted as follows for the particular value of $E = 10^{-4}$ of the example shown, the first well-defined mode is $m = 8$. The flow then undergoes a sequence of mode transitions to $m = 6, 4, 3$, and 2. Other transitions, e.g. to modulation, are only seen for wavenumbers 2 or less. Reversing the bifurcation parameter resulted in a similar sequence, though considerable hysteresis is found. In the reversal of the experiment discussed here for instance, the highest wavenumber found was $m = 5$.

The relationship between m and W_1 in (5.1) suggests a dispersion relation for the wave speed, $\omega_m = c_m k$, as

$$\omega_m = (0.89 - 1.08/m)\omega/2 \tag{5.2}$$

with $\omega_m = 2\pi f_1/m$. No systematic variation with the background rotation Ω could be detected. Equation (5.2) implies that all waves drift slower than the mean shear flow ($\omega/2$) where the retardation is strongest for the low wavenumbers. This was also noted by Rabaud & Couder (1983) who argued that the retardation was caused by the fact that the vortices were not central in the shear layer but shifted to the outside. This observation was also made in our flow visualization experiments such as in figure 9. Furthermore, the lower wavenumbers had a larger radial dimension and a more pronounced outward shift. Therefore, all vortices would drift at a velocity between

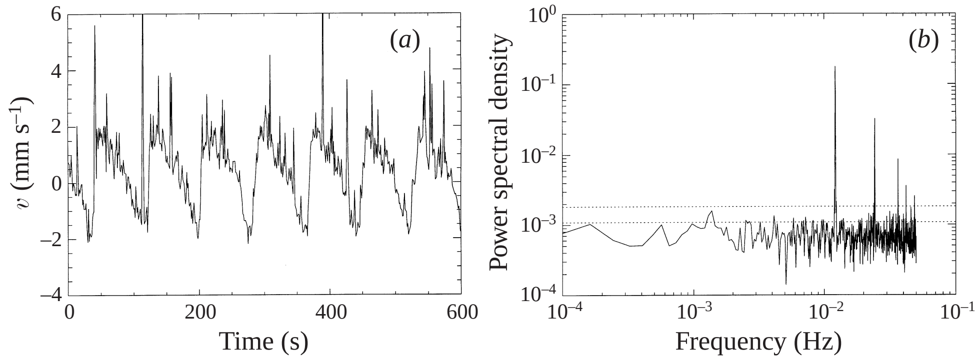

FIGURE 13. (a) Short segment of a time series of the radial velocity, and (b) power spectrum for noisy vortices, $nV4$.

that of the outer section of the tank (stationary in our measurement frame) and the mean shear flow, where the influence of the stationary outer section would become stronger with increasing vortex diameter. The empirical dispersion relation found by Rabaud & Couder (1983) and Chomaz *et al.* (1988), namely $\omega_m = (1 - 1.4/m)\omega/2$ (transformed to our coordinate system), agrees qualitatively with (5.2).

The wavenumbers observed at the onset of instability cover the predicted range of Niino & Misawa (1984) for the most unstable wave mode extremely well, from $m = 8$ at the smallest possible values of the Ekman number, to $m = 3$ at the largest values of E. In figure 12(b), the first reliable wavenumber as found from frequency plots such as figure 12(a), is plotted as a function of the Ekman number, together with the most unstable wavenumber as predicted by quasi-geostrophic theory.

5.3. *Noisy vortices*

The vast majority of the experiments in the vortex regimes showed some noise up to $\approx 1\,\mathrm{mm\,s^{-1}}$ which is well above the measurement noise level of the LDV system ($\approx 0.2\,\mathrm{mm\,s^{-1}}$). This noise, however, was not detectable by the particle tracking experiments. As shown in the times series of $nV4$ in figure 13(a), the 'noisy' flows not only exhibited an increased level of relatively uniform fluctuations (about 1 mm s^{-1} in the displayed example), but also frequent spikes in the signal of the same order of magnitude as the vortex signal itself. The flow in figure 13 is an $m = 4$ flow, the same as the regular flow $V4$ shown in figure 10, and it was observed at $(Ro, E) = (-0.16, 3\times10^{-4})$, very close to the regular flow at $(Ro, E) = (-0.18, 3\times10^{-4})$, after a transition from $m = 5$ at $Ro \approx -0.13$. The power spectrum, in figure 13(b), only shows the vortex drift at $f_1 = 1.216 \times 10^{-2}$ Hz and its harmonics.

Phase space reconstructions using singular systems analysis showed the same loss of signal-to-noise ratio, as shown in figure 14. The fuzzy but thin toroidal structure of V has a singular spectrum where the first two eigenvectors captured 76% of the variance and the first two pairs 94% (figure 15a), while for nV the first pair of eigenvectors described only 36% of the total variance and the first four eigenvectors 46% (figure 15b). The singular spectrum of the noisy vortex flow shows some apparently paired eigenvectors 3 and 4, which is often indicative of oscillatory modes, but their respective principal components do not show any resolvable structure in the phase portraits as illustrated in the return map of the positive crossings of the second principal component of the Poincaré section where the first principal component is zero in figure 14(b). The only ordered structure in the reconstructed phase space

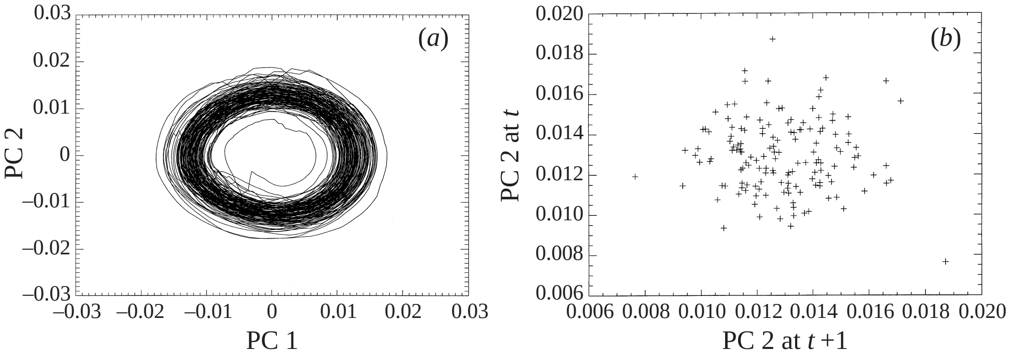

FIGURE 14. (*a*) Phase portrait and (*b*) return map of second principal component for the noisy vortex flow $nV4$.

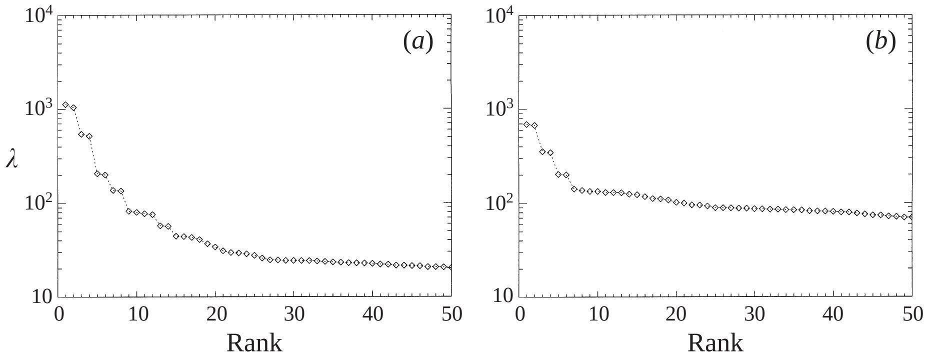

FIGURE 15. Singular spectra from SSA (*a*) for $V4$, and (*b*) for $nV4$, both with a window length of 80 s.

is the large oscillation of the first pair of eigenvectors, associated with the vortices drifting past the measurement point (figure 14*a*). Also, the dimension estimates failed to show any scaling region: the limit cycle from the first pair of eigenvectors did not contribute to even a small scaling region.

A way to detect if there may be any additional structure hidden in the noise besides the strong vortex signal is to use the reference SSA technique, R-SSA, as described in § 2.2.2. Figure 16 shows the singular spectrum of $nV4/V4$, in which the periodic motion and the background noise found in V have been filtered out. The resulting flat spectrum which is well below the calculated noise level (indicated by the solid line in figure 16) can be interpreted in the following way: the vortex dynamics, which in the standard SSA resulted in the strong first pair of eigenvectors, are accounted for in the reference model and do not appear as a 'new' signal in the filtered noisy data. The second pair of eigenvectors, which had quite substantial eigenvalues without showing any structure in the phase portrait, does not contain any coherent signal above the noise level, once the periodic solution is filtered out. Only a flat white noise spectrum remains. The conclusion is that the noisy vortices do not contain any more information or further deterministic dynamics (as could have been indicated by the enhanced eigenvalues of the second pair of eigenvectors), but that the noisy vortex state contains the same deterministic dynamics as the periodic vortices only with added white noise.

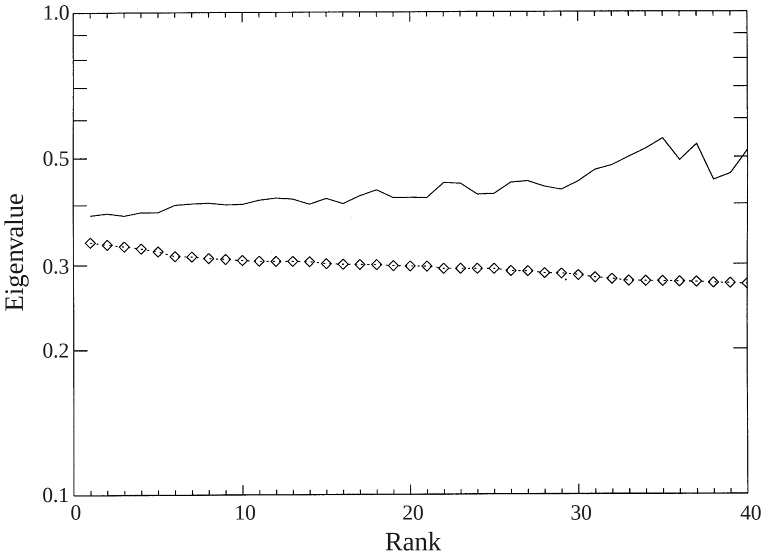

FIGURE 16. Singular spectra for $nV4/V4$ using R-SSA with a window length of 80 s. The singular values are the diamonds while the solid line is the noise level computed from the reference signal in the respective eigenvector.

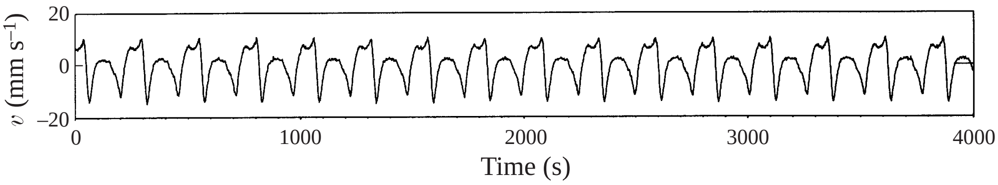

FIGURE 17. Time series of radial velocity for period-doubled case Pa.

5.4. *Period-doubling*

No true $m = 1$ flow was found in the experiment. Instead, the velocity signal developed a strong period-doubled signature and so this flow type is labelled P. Unlike the other regular vortex flows which showed in most cases a significant noise contribution, periodic flows with very little noise covered a much larger area of the regime diagram than noisy P flows. The latter were found relatively close to the irregular regimes, though sequences from I to periodic P and then to noisy P were found and are discussed separately in § 5.5.

Figure 17 shows the time series of Pa, a typical period-doubled flow. From the phase portrait reconstruction in figure 18 it seems that Pa is a regular period-doubled flow. A window length of 140 s was used which extended over the period of the main oscillation of 127 s but not over the period-doubled period of 254 s.

Flow visualization experiments, as shown in figure 19, have revealed that this flow is in fact a steady vortex flow which could be described as a spatially period-doubled flow with strong $m = 1$ and $m = 2$ components of one strong and one weak vortex in a distorted jet stream. The two vortices are not at opposite sides of the centre of the tank, as it was the case in the $m = 2$ flow, but the lines from the tank centre to the centre of each vortex form an angle of 37° in the case of figure 19. Other particle tracking experiments across the P regime showed considerable variation of this angle

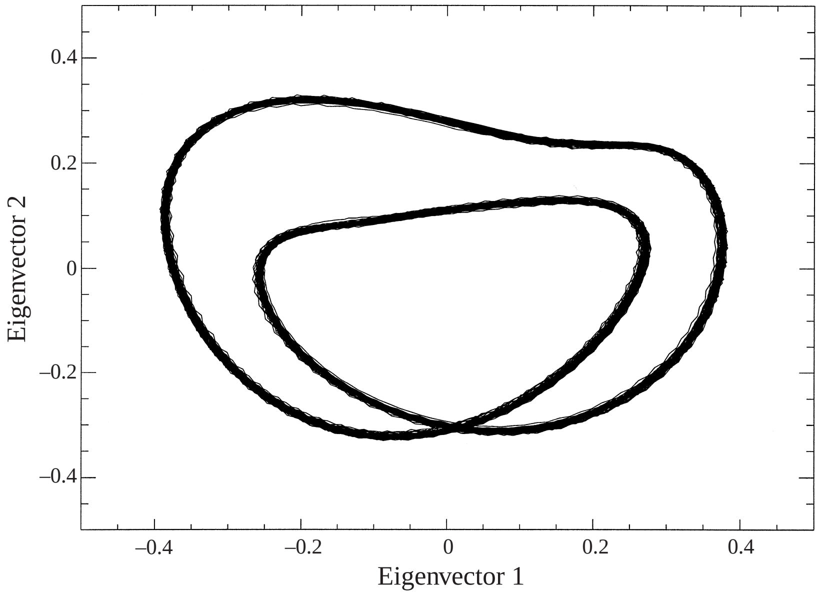

FIGURE 18. Phase portrait of period-doubled vortex flow Pa.

from less than 10° up to about 45°. Once this flow pattern was established, it was very stable over a large range of parameters, with very little noise.

5.5. *Anomalous P flow*

Co-existing with the periodic P flows, other complex flow regimes were observed close to the irregular flow. These complex flows developed from a periodic flow which appeared to be almost identical to the standard P flows. A comparison of the time series of two period-doubled flows, Pa and Pi, in figures 17 and 20(*a*), reveals that Pi is a mirror image Pa through $v \mapsto -v$. The inverted flow, Pi, was found only after spinning up the experiment from rest, while the standard form was also found at the same point in parameter space when ramping from the irregular flow or regular vortices.

While the inversion of the radial velocity does not correspond to a symmetry of the cylindrical flow, it is part of some symmetry operations under which a shear layer in a straight channel would be invariant. If the radius of the shear layer is much larger than its thickness, then the layer could be locally approximated by a straight layer. Under those circumstance it is possible that some of the symmetries, and with them symmetric flow types, may be valid for some regions in the parameter space. During the particle tracking experiments, no anomalous P flow was found, but to test if any of the possible symmetry operations of the straight channel case would give a reasonable flow structure in the circular tank, a velocity field from the standard P flow, as presented in figure 19 was taken, and several symmetry operations were performed on the eddy field, after the mean azimuthal velocity was subtracted. The following symmetry operations were tested: (*a*) $(y, v) \mapsto -(y, v)$, (*b*) $(y, u, v) \mapsto -(y, u, v)$, and (*c*) $(u, v) \mapsto -(u, v)$, where $y = r - R$ is the radial (lateral) distance from the shear layer centre, and $u = U - \overline{U}$ and v are the azimuthal and radial velocity components. Of these three combinations, the last, $(u, v) \mapsto -(u, v)$ resulted in the most plausible flow structure which is shown in figure 21.

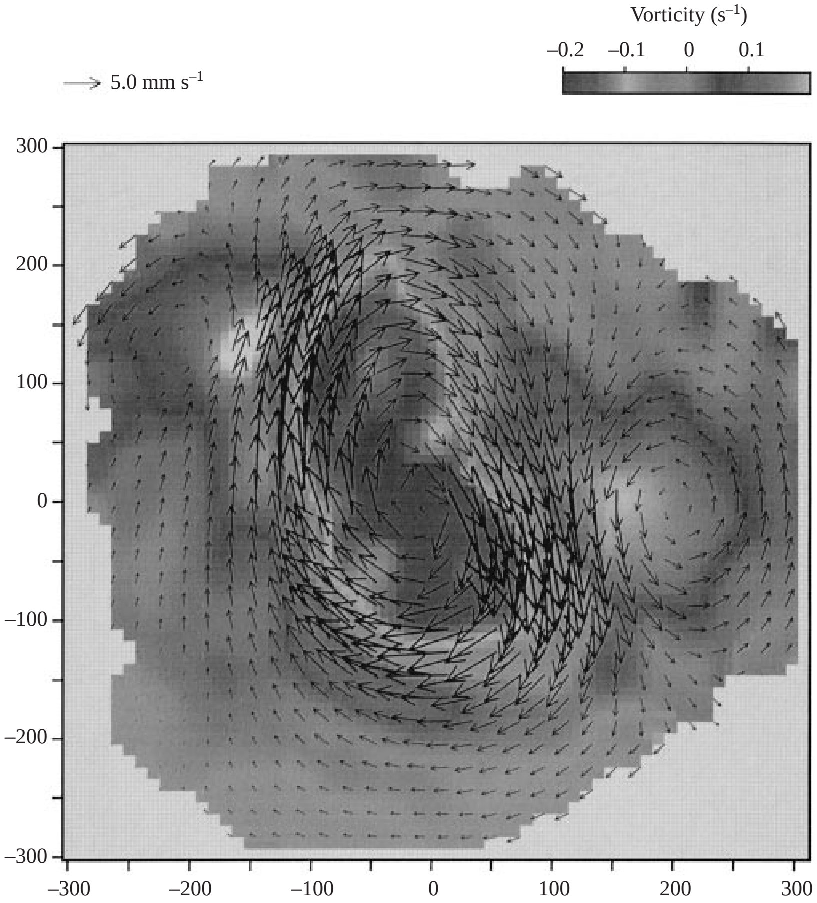

FIGURE 19. Velocity field and vorticity map of 'period-doubled' flow Pb at $Ro = -0.50$ and $E = 7.3 \times 10^{-4}$.

Following from Pi, the inverted flow mPi developed strong fluctuations shown in figure 20(*b*). The corresponding power spectra of the periodic and irregular flows are shown in figure 22. The spectrum of the periodic flow shows the dominant frequency, its subharmonic and even indications of a period four besides the higher harmonics above a very small noise level. mPi, on the other hand, shows a much greater noise level falling off towards higher frequencies akin to a red noise spectrum, as well as a distinct peak at $f = 2.67 \times 10^{-2}$ Hz or $W = 2.05$. This frequency, which is 3.73 times larger than the frequency of the long wave ($W = 0.55$), does not correspond to an observed drift frequency of another mode and seems therefore to be a temporal modulation.

While standard SSA analysis of Pi results in the expected slow oscillation in the leading pair of singular vectors, the corresponding vectors for mPi in figure 23(*a*) show a two-frequency oscillation where the phase space of mPi shows a complex phase portrait of the two frequencies convolved. Instead of a pair of singular vectors with similar variance, the singular spectrum in figure 23(*c*) shows four leading eigenvectors, each containing information from both frequency components. Filtering the slow oscillation out by using R-SSA with Pi as the contamination signal succeeds in isolating the fast oscillation: a distinct pair of leading singular vectors is well above

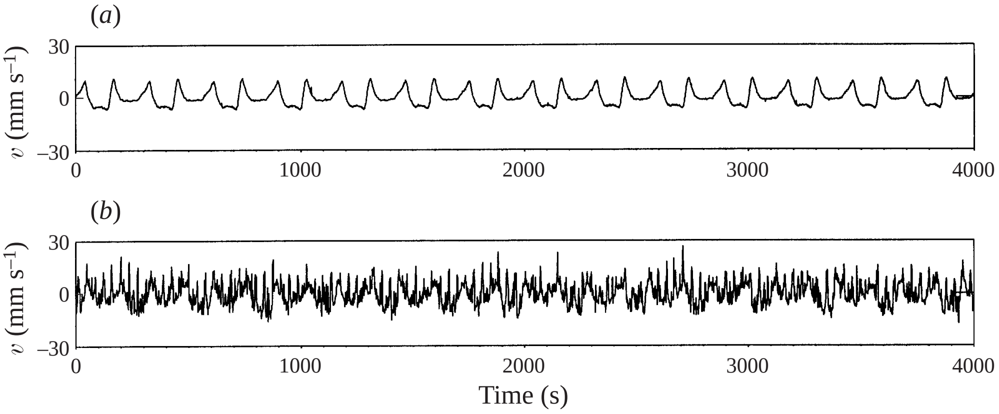

FIGURE 20. Time series of radial velocity for (*a*) anomalous period-doubled case Pi, and (*b*) noisy modulated case mPi.

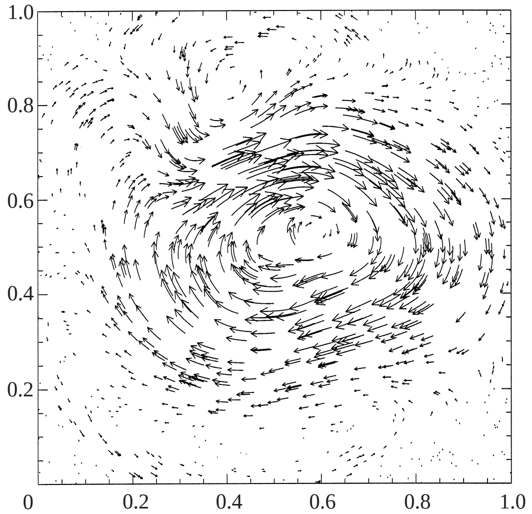

FIGURE 21. Velocity field of an inverted period-doubled flow constructed by the inversion of the perturbation velocities from Pb around the centreline of the axisymmetric shear layer.

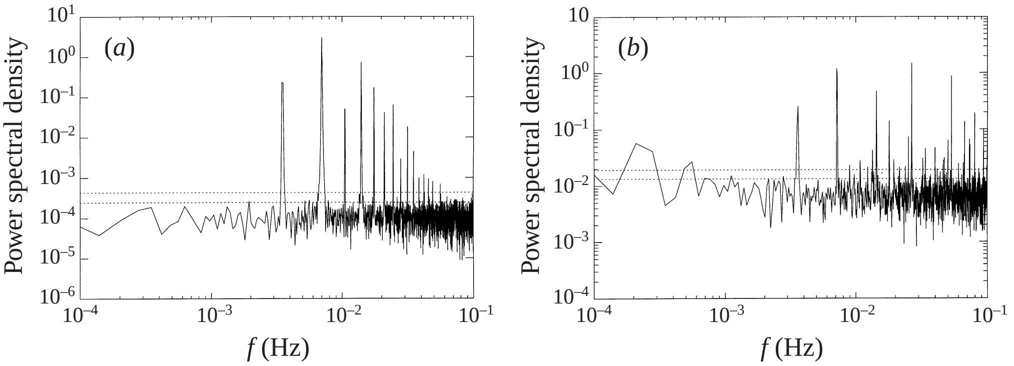

FIGURE 22. Power spectra of radial velocity time series for (*a*) Pi, and (*b*) mPi.

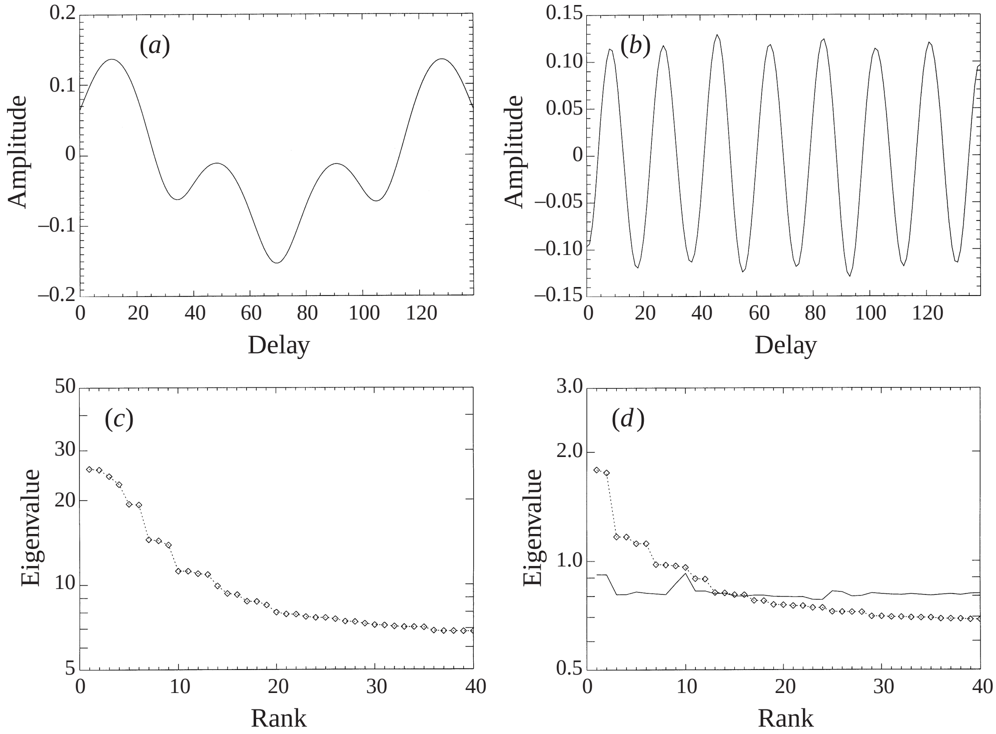

FIGURE 23. (*a*) First singular vector of *mPi* using standard SSA using a window length of 140 s, and (*b*) leading singular vector of *mPi*/*Pi* from R-SSA with a window length of 140 s. (*c*) The first 40 singular values of the singular spectrum for the standard SSA of *mPi*. (*d*) The singular spectrum for R-SSA of *mPi*/*Pi*.

the calculated noise level as shown in figure 23(*d*). Figure 23(*b*) shows the first singular vector of *mPi*/*Pi*, in which the fast oscillation is now clearly visible. The phase portrait of this oscillatory mode recovers a noisy limit cycle similar to that of *nV*4 (cf. figure 14). As the singular vector in figure 23(*b*) shows, the period of the fast oscillation is 18.7 s, half of the period found in the power spectrum in figure 22.

It appears that this flow is on a solution branch disconnected from the other solutions, which could be stabilized for a finite range of parameters by virtue of a near-symmetry with respect to left–right inversion centred on the shear layer. The standard period-doubled flow does not show the breakdown to a faster modulation and occurrence of noise, but remains stable for a large range of parameters before undergoing further bifurcations leading to a slower modulation of the flow structure.

6. Conclusions

We have presented results from a laboratory study of the instability and nonlinear dynamics of a rotating flow subjected to a horizontal shear. This study has addressed in some detail the conditions under which the Stewartson layer due to symmetric forcing at the upper and lower boundaries becomes unstable. Our analysis has shown that instability sets in at a well defined Reynolds number. This lends further evidence in support of the validity of the quasi-geostrophic approximation used in the theoretical study by Niino & Misawa (1984). Even though this approximation resolves neither any vertical structure (apart from Ekman layers) nor the $E^{1/3}$ layer, its predictions were reproduced remarkably well in the experiments. In contrast to this, boundary layer approaches, such as Busse (1968) or Hashimoto (1976), did not predict the existence of a stable axisymmetric flow. It appears that the inclusion of internal diffusion in the fluid interior is crucial in providing a short-wave cut-off and thus a lower limit for the growth of perturbations. The marginal stability can be defined by a critical Reynolds number, $Re_{i,c} = 19E^{-0.03}$. This Reynolds number is based on the thickness of the $E^{1/4}$ Stewartson layer and is a measure of the shear across the layer (U/L where $U = R\omega$ and $L = E^{1/4}H$) relative to the molecular dissipation (ν/L^2). This suggests that the effect of rotation on the inertial instability of the basic flow is indirect by concentrating the shear in a layer of thickness $E^{1/4}$. The experiments by Rabaud & Couder (1983) on a circular shear layer without strong background rotation showed a critical Reynolds number (based on H rather than $E^{1/4}H$, since they used parameters with $E \geqslant 1$) of $Re_c \approx 85$–110. Niino & Misawa (1984) and Solomon *et al.* (1993) also studied the instability of a jet stream with a similar value for a critical Reynolds number. Solomon *et al.* (1993), whose experiments were on a β-plane, found a small difference of the critical value between co-rotating and counter-rotating jets due to the β-effect, which is consistent with theoretical results by Marcus & Lee (1998).

This study is the first to provide firm evidence that the nature of the transition is that of a supercritical instability through a Hopf bifurcation. The flow structures emerging from the Hopf bifurcation are travelling waves in the form of a wavy shear layer together with a string of vortices along the shear layer, where the range of wavenumbers observed (up to $m = 8$) is well predicted by quasi-geostrophic theory. As with the onset of instability, the resulting flow growing from this instability does not seem to vary strongly with the sign of ω. While this invariance is consistent with the findings by Rabaud & Couder (1983) and Solomon *et al.* (1993), it is in contrast to those of Hide & Titman (1967) who reported flows with wavenumbers 2 or greater only for positive Ro. For $Ro < 0$, however, they only observed a unique flow structure which was described as a distorted and displaced ellipsoidal jet stream which could be consistent with the spatially period-doubled flow structure P described in § 5.4. The main difference between the studies is that Hide & Titman placed the differentially rotating disk in the fluid interior at mid-height rather than at the boundaries. It appears that the sudden jump in the fluid depth across the edge of the disk may have caused this marked difference of the flow structures between the different signs of the disk rotation. A recent numerical study by R. Hollerbach (1998, personal communication) in a spherical shell with a similar depth change across the shear layer also found a difference between the directions of the relative rotation. The Taylor–Couette system also shows strong differences between co- and counter-rotating cylinders (Andereck, Liu & Swinney 1986). One of the primary forces in the Taylor–Couette system is the centrifugal force which depends crucially on the relative rotation. The absence of major differences between the signs of the disk rotation in the present experiment would indicate that centrifugal forces can be neglected in the initial instability and for a large range of the parameter space explored.

Though there are some differences in the regimes observed for positive and negative Ro, the general structure of the regime diagram appears to be independent of the sign of Ro. The lines of mode transitions and the structures of the more complex flows, M and I, are more regular for positive Ro. In both cases, however, the mode transitions appear to depend mainly on Ro rather than E. This is not only reflected by other shear layer experiments, e.g. Hide & Titman (1967), but it is also observed in the baroclinic rotating annulus, e.g. Hide & Mason (1975). The principal parameters in the baroclinic experiment are a thermal Rossby number, Θ, and a Taylor number, $\mathcal{T} \propto E^{-2}$. A typical regime diagram, such as figure 7 in Hide & Mason (1975), shows that mode transitions to higher modes are usually found when Θ is decreased.

While secondary instabilities are a common occurrene in both the baroclinic annulus (e.g. Früh & Read 1997) and in the Taylor–Couette flow, this shear layer experiment showed only very few indications of secondary instabilities, all restricted to the lower wavenumbers, $m \leqslant 3$. The most typical secondary instability of a baroclinic wave is that of a secondary Hopf bifurcation to a so-called amplitude vacillation, with further bifurcations predominantly involving homoclinic orbits. Those complex flows are usually found in the baroclinic annulus before a transition to a lower wavenumber. Mode transitions in this experiment, however, were not preceded by bifurcations to chaotic flows, although enhanced levels of noise were observed near transitions to either lower or higher wavenumbers. No indications were found that these fluctuations could be a result of low-dimensional nonlinear dynamics. The only indications of a strong second independent frequency and further bifurcations were found for low wavenumbers, $m \leqslant 2$, especially in the modulated regime m and the spatially period-doubled flow P. The modulated flow could be an amplitude oscillation of an $m = 2$ mode or a nonlinear interference of an $m = 2$ and an $m = 3$ mode. These flows, however, and the islands of sudden strong irregular behaviour are still poorly understood and are the focus of Part 2.

This research was funded by a research grant from the UK Natural Environment Research Council (NERC). We would like to express our thanks to the workshops in the Clarendon Laboratory and the Atmospheric Physics Department, Oxford, for their help in designing and manufacturing the experimental apparatus. We are indebted to Professor Raymond Hide and the late Professor David Tritton for inspiring discussions and valuable comments.

REFERENCES

Allen, M. R. & Smith, L. A. 1997 Optimal filtering in singular systems analysis. *Phys. Lett.* A **234**, 419–428.

Andereck, C. D., Liu, S. S. & Swinney, H. L. 1986 Flow regimes in a circular Couette system with independently rotating cylinders. *J. Fluid Mech.* **164**, 155–183.

Antipov, S. V., Nezlin, M. V., Snezhkin, E. N. & Trubnikov, A. S. 1986 Rossby autosoliton and stationary model of the Jovian Great Red Spot. *Nature* **323**, 238–240.

Baker, J. D. 1967 Shear layers in a rotating fluid. *J. Fluid Mech.* **29**, 165–175.

Broomhead, D. S. & King, G. P. 1986 Extracting qualitative dynamics from experimental data. *Physica* D **20**, 217–236.

Busse, F. H. 1968 Shear flow instabilities in rotating systems. *J. Fluid Mech.* **33**, 577–589.

Chomaz, J. M., Rabaud, M., Basdevant, C. & Couder, Y. 1988 Experimental and numerical investigation of a forced circular shear layer. *J. Fluid Mech.* **187**, 115–140.

Dalziel, S. B. 1992 Decay of rotating turbulence: some particle tracking experiments. *J. Appl. Sci. Res.* **49**, 217–244.

Früh, W.-G. & Read, P. L. 1997 Wave interactions and the transition to chaos of baroclinic waves in a thermally driven rotating annulus. *Phil. Trans. R. Soc. Lond.* A **355**, 101–153.

Grassberger, P. & Procaccia, I. 1983 Characterization of strange attractors. *Phys. Rev. Lett.* **50**, 346–349.

Greenspan, H. P. 1968 *The Theory of Rotating Fluids*. Cambridge University Press.

Guckenheimer, J. & Buzyna, G. 1983 Dimension measurements for geostrophic turbulence. *Phys. Rev. Lett.* **51**, 1438–1441.

Hashimoto, K. 1976 On the stability of the Stewartson layer. *J. Fluid Mech.* **76**, 289–306.

HIDE, R. & MASON, P. J. 1975 Sloping convection in a rotating fluid. *Adv. Phys.* **24**, 47–99.

HIDE, R. & TITMAN, C. W. 1967 Detached shear layers in a rotating fluid. *J. Fluid Mech.* **29**, 39–60.

HOLLERBACH, R. 1996 Magnetohydrodynamic shear layers in a rapidly rotating plane layer. *Geophys. Astrophys. Fluid Dyn.* **82**, 237–253.

HOLTON, J. R. 1971 An experimental study of forced barotropic Rossby waves. *Geophys. Fluid Dyn.* **2**, 323–341.

HUMPHREY, J. A. C. & GOR, D. 1993 Experimental observations of an unsteady detached shear layer in enclosed corotating disk flow. *Phys. Fluids* A **5**, 2438–2442.

KNOBLOCH, E. 1996 Symmetry and instability in rotating hydrodynamic and magnetohydrodynamic flows. *Phys. Fluids* **8**, 1446–1454.

MARCUS, P. S. & LEE, C. 1998 A model for eastward and westward jets in laboratory experiments and planetary atmospheres. *Phys. Fluids* **10**, 1474–1489.

MEYERS, S. D., SOMMERIA, J. & SWINNEY, H. L. 1989 Laboratory study of the dynamics of Jovian-type vortices. *Physica* D **37**, 515–530.

MULLIN, T. (ed.) 1993 *The Nature of Chaos*. Clarendon Press.

NEZLIN, M. V., RYLOV, A. Y., TRUBNIKOV, A. S. & KHUTORESTKIĬ, A. V. 1990 Cyclonic-anticyclonic asymmetry and a new soliton concept for Rossby vortices in the laboratory, oceans and the atmospheres of giant planets. *Geophys. Astrophys. Fluid Dyn.* **52**, 211–247.

NIINO, H. & MISAWA, N. 1984 An experimental and theoretical study of barotropic instability. *J. Atmos. Sci.* **41**, 1992–2011.

RABAUD, M. & COUDER, Y. 1983 A shear-flow instability in a circular geometry. *J. Fluid Mech.* **136**, 219–319.

READ, P. L. 1992 Long-lived eddies in the atmospheres of the major planets. In *Rotating Fluids in Geophysical and Industrial Applications* (ed. E. J. Hopfinger), ch. v.3, pp. 283–299. Springer.

READ, P. L., BELL, M. J., JOHNSON, D. W. & SMALL, R. M. 1992 Quasi-periodic and chaotic flow regimes in a thermally-driven, rotating fluid annulus. *J. Fluid Mech.* **238**, 599–632.

RUELLE, D. 1973 Bifurcations in the presence of a symmetry group. *Arch. Rat. Mech. Anal.* **51**, 136–152.

SCHÄR, C. & DAVIES, H. C. 1990 An instability of mature cold fronts. *J. Atmos. Sci.* **47**, 929–950.

SIMMONS, A. J. & HOSKINS, B. J. 1978 The life cycles of some nonlinear baroclinic waves. *J. Atmos. Sci.* **35**, 414–432.

SOLOMON, T. H., HOLLOWAY, W. J. & SWINNEY, H. L. 1993 Shear flow instabilities and Rossby waves in barotropic flow in a rotating annulus. *Phys. Fluids* A **5**, 1971–1982.

STEWARTSON, K. 1957 On almost rigid rotations. *J. Fluid Mech.* **3**, 17–26.

WEBER, H. C. & SMITH, R. K. 1993 The stability of barotropic vortices – implications for tropical cyclone motion. *Geophys. Astrophys. Fluid Dyn.* **70**, 1–30.

WOLF, A., SWIFT, J. B., SWINNEY, H. L. & VASTANO, J. A. 1985 Determining Lyapunov exponents from a time series. *Physica* D **16**, 285–317.